Archives of Acoustics Vol. 48, No. 4, pp. 475–495 (2023), doi: 10.24425/aoa.2023.146812

Research Paper

Research on the Performance Optimization of Turbulent Self-Noise Suppression and Sound Transmission of Acoustic Windows Made from Functionally Graded Material

Bing LI, Fu-Lin ZHOU*, Jun FAN, Bin WANG, Li-Wen TAN

Key Laboratory of Marine Intelligent Equipment and System, Ministry of Education
P.R. China

*Corresponding Author e-mail: zhoufulin@sjtu.edu.cn

(*received September 29, 2022; accepted April 14, 2023*)

For a simplified sonar dome model, an optimization method for internal gradients of functionally graded material (FGM) acoustic windows is proposed in this paper. This method can be used to design optimized FGM acoustic windows with better turbulent self-noise suppression and sound transmission performances. A theoretical model of FGM acoustic windows to evaluate the reduction of self-noise caused by the turbulent boundary layer (TBL) pulsating pressure and the sound transmission loss (STL) is derived through the double Fourier transform and the wavenumber frequency spectrum analysis, respectively, based on the transfer matrix idea and the classical elastic theory. The accuracy of the theory is verified by the finite element results of COMSOL Multiphysics. Utilizing the genetic algorithm (GA) and taking the monotonic gradient as the constraint condition, the internal gradient optimization method of FGM acoustic windows obtains the optimization variables in the Bernstein polynomial when the optimization objective is minimized by iterating the optimization variables in the deviation function represented by the Bernstein polynomial that is introduced in the gradient function. The STL, the turbulent self-noise reduction or a weighting function of the STL and turbulent self-noise reduction of FGM acoustic windows is chosen as the optimization objective. The optimization calculation of the sound transmission or turbulent self-noise suppression performances is carried out for the FRP-rubber FGM (FGM with fiber reinforced plastic (FRP) as the substrate material and rubber as the top material) acoustic window. The optimized results show that both the sound transmission and turbulent self-noise suppression performance are effectively improved, which verifies the effectiveness of the optimization method. Finally, the mechanism of the sound transmission and self-noise suppression characteristics before and after optimization are explained and analyzed based on the equivalent model of graded materials. The research results of this paper provide a reference value for the future design of FGM acoustic windows for sonar domes.

Keywords: functionally graded material; acoustic window; turbulent self-noise; sound transmission loss; optimization.

1. Introduction

When underwater vehicles operate, a sound permeable enclosure, which is known as the sonar dome, is usually configured outside the sonar array to avoid the impact of water flow on the array and prevent direct interference from exposure to turbulent self-noise (Lavender, 1994; Srivastava, 1998). The suitable design of a sonar dome ensures sufficient strength and a favorable linear shape but requires good sound transmission and turbulent self-noise suppression performance; in particular, the sound transmission loss (STL) of the external acoustic signal or the transmitting signal of the internal matrix should be reduced as much as possible. The turbulent self-noise suppression characteristics require that the acoustic window can suppress "pseudo-sound", that is, filter out the structural vibration noise caused by external turbulence. Early designs of acoustic windows used stainless steel, but the turbulent self-noise suppression char-

acteristics were poor. In the 1970s and 1980s, the subsequent use of rubber material improved the turbulent self-noise reduction, but the stiffness was not sufficient. Currently, fiber reinforced plastic (FRP) is mostly used as an acoustic window material with good sound transmission performance and strong stiffness; however, its turbulent self-noise reduction needs to be improved (Hoffmann, 1998; Burton, 1998). Scholars have found that the effect of multilayer composite plates is better than that of single-layer structures in terms of both sound transmission and turbulent self-noise suppression performance. Compared with a single material, a composite plate can benefit from the advantages of different materials (Cremer *et al.*, 2005; Ham *et al.*, 2018; Lee *et al.*, 2010; Yu *et al.*, 2005) and thus, can provide more performance improvements. However, the impedance discontinuities at the interfaces of different materials have a certain influence on the acoustic-vibration characteristics of simple sandwich composite plates.

The functionally graded materials (FGMs) (Mortensen, Suresh, 1995; Pompe *et al.*, 2003; Liu *et al.*, 2004; Prakash, Ganapath, 2006), which are widely used in the fields of aviation, optics, and energy, have smooth and continuous material properties along the thickness direction, can achieve continuous impedance transitions and impedance connection matching, and can potentially be applied in acoustics (Lane, 1981). There have been few studies on the sound transmission characteristics and turbulent self-noise suppression characteristics of FGMs; and most studies have focused on structural acoustic radiation (George *et al.*, 2016; Hosseini-Hashemi *et al.*, 2010; Zhao *et al.*, 2009; Iqbal *et al.*, 2009; Kumar *et al.*, 2009). Shang (1965) studied the acoustic reflection performance of a gradual absorption layer in 1965, deduced a general expression for acoustic reflection of a gradual absorption layer, and concluded that an absorption layer with a linear gradual change in material parameters provided good acoustic absorption performance. Chandra *et al.* (2014; 2015) used a simple first-order shear deformation theory to investigate the displacement, velocity, acceleration, radiated sound level, radiated sound pressure level and radiated efficiency of FGM plates with power-law exponential changes. The acoustic transmission loss of FGMs with different incident angles and power-law exponents was studied in detail. The simulation results showed that the transmitted sound power level increased monotonically with an increasing power index in the low frequency range of 0–500 Hz, with a difference of more than 10 dB(A). Rabbani *et al.* (2019) established a thick-walled FGM cylindrical shell theory model to solve the deformation and stress in cylindrical shells by using the state space method based on the three-dimensional elastic theory and the piezoelectric elastic theory and calculated the acoustic transmission loss caused by the piezoelectric effect of thick-walled piezoelectric composite cylindrical shells under plane wave excitation. The results were verified through COMSOL. In the area of turbulent self-noise suppression, Zhou *et al.* (2020) used FGM to carry out research on sonar self-noise reduction. The Corcos model, which considered the excitation source of the sonar structure, was adopted to establish a hydrodynamic noise prediction model of a uniformly coated layer and conduct research on turbulent self-noise reductions. The effect of FGM on the turbulent self-noise suppression performance was analyzed for four typical distribution characteristics: linear, parabolic, power-law, and exponential functions. According to the literature results, FGMs have good research prospects in both sound transmission and turbulent self-noise suppression. However, these characteristics have not previously been considered simultaneously in previous FGM research.

In this paper, the turbulent self-noise suppression and sound transmission characteristics of acoustic windows made from FGM are studied simultaneously for the sonar dome. Through the internal gradient optimization design, optimized FGM acoustic windows with better turbulent self-noise suppression and sound transmission performance are obtained. The main sections are arranged as follows. In Sec. 2, based on the classical elastic theory and the transfer matrix, a theoretical model on FGM acoustic windows to evaluate the turbulent self-noise caused by external turbulent boundary layer (TBL) pulsating pressure and STL towards an incident plane wave is derived utilizing the double Fourier transform and the wavenumber-frequency analysis, and the accuracy is verified by the finite element results of COMSOL Multiphysics. In Sec. 3, specific internal changes in the gradient optimization method for FGM acoustic windows are proposed based on the twin consideration of the turbulent self-noise suppression and sound transmission performance, which enables design of an optimized FGM acoustic window with higher turbulent self-noise reduction and lower STL. In the optimization method, a monotonic gradient is taken as the constraint condition. Upon combining a genetic algorithm (GA), five optimization variables in the Bernstein polynomial, when the optimization objective is minimized, are obtained by iterating optimization variables in the deviation function represented by the Bernstein polynomial introduced in the gradient function. The optimization objective is expressed as the STL, the turbulent self-noise reduction or a twin weighting function of the STL and turbulent self-noise reduction of FGM acoustic windows. In Sec. 4, optimization calculations of the sound transmission or turbulent self-noise suppression performances are carried out for an FRP-rubber FGM based on the proposed gradient optimization method. In Sec. 5, the mechanism of the sound transmission

and turbulent self-noise suppression characteristics of the FRP-rubber FGM acoustic window before and after optimization are explained based on the spectral method and a thin-plate model, using the equivalent model of graded materials. In Sec. 6, the conclusion is provided.

2. Theory model of turbulent self-noise and STL for a simplified sonar dome with FGM acoustic windows

The sonar dome structurally consists of an acoustic window, a cavity in the dome and a sonar array surface; a simplified two-dimensional sonar dome model (Yu *et al.*, 2005; Maidanik, 1968; Crighton *et al.*, 1992) composed of flat plates and parallel cavities can be adopted. In this model, the acoustic window is a flat plate made from FGM. Because the material properties of FGM change with thickness, the most efficient method to calculate the vibro-acoustic performance is to use discrete N-layer approximation materials. Each layer is an infinitely homogeneous and isotropic medium. The cavity between the sonar array and the acoustic window is idealized as a liquid layer. The sonar array surface is idealized as a plane with a surface acoustic reflection coefficient of R. Outside the sonar dome is a semi-infinite acoustic medium, which is affected by a stationary random TBL pulsating pressure and an incident plane wave. The theoretical analysis model and the x-z coordinate system of the sonar dome are shown in Fig. 1. The thickness of the acoustic window is H, the total number of layers is N, and the index is numbered from the outer surface ($z = 0$) to the inner surface ($z = H$) of the dome. The 1st layer, i.e., the upper interface, is called the top layer (symbol t). The N-th layer, i.e., the lower interface, is called the base (symbol b). The external water layer is the 0 layer. The sonar cavity water layer is the N+1 layer with height L. The time factor is $e^{-i\omega t}$.

Here, p_{in} is the incident plane wave with an incident angle θ_i; p_r within a reflection angle θ_r and p_t with a refraction angle θ_t are the reflected wave and the sonar cavity acoustic field caused by the incident plane wave, respectively; and p_0 and p_{N+1} are the external acoustic field and the sonar cavity acoustic field caused by the TBL pulsating pressure F, respectively. According to the principle of linear superposition, the self-noise caused by the TBL pulsating pressure F and the transmission acoustic field caused by the external sound source can be calculated separately.

2.1. Theoretical model of the wavenumber-frequency response function of the turbulent self-noise excited by TBL pulsating pressure

Although the TBL pulsating pressure F is random in time and space, it is stable and fixed in the wavenumber-frequency space after statistical analysis. Therefore, the sonar self-noise caused by the TBL pulsating pressure F is calculated as the vibration-acoustic radiation in the wavenumber-frequency space. The double Fourier transform of the TBL pulsating pressure F on the acoustic window is:

$$F(x,z,t) = \frac{1}{(2\pi)^2} \iint_{-\infty} \widetilde{F}(k,\omega,z) e^{i(kx-\omega t)} \,\mathrm{d}k \,\mathrm{d}\omega, \quad (1)$$

where $\widetilde{F}$ is the excitation force amplitude in the wavenumber space, k is the wavenumber in the x-direction, and ω is the angle frequency. For the medium from 0 to N+1, the velocity potential function must satisfy the scalar or vector wave equation:

$$\begin{aligned} \frac{\partial^2 \phi}{\partial x^2} + \frac{\partial^2 \phi}{\partial z^2} &= \frac{1}{c_L^2} \frac{\partial^2 \phi}{\partial t^2}, \\ \frac{\partial^2 \psi}{\partial x^2} + \frac{\partial^2 \psi}{\partial z^2} &= \frac{1}{c_T^2} \frac{\partial^2 \psi}{\partial t^2}, \end{aligned} \quad (2)$$

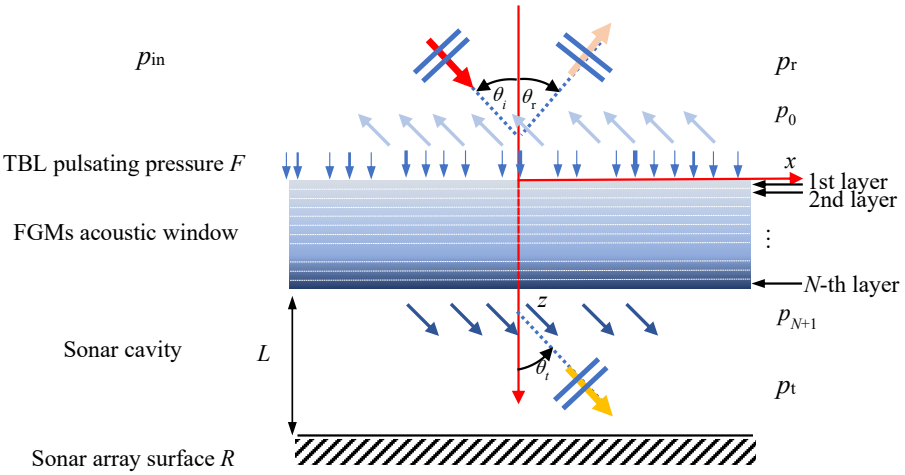

Fig. 1. Theoretical analysis model of the simplified two-dimensional sonar dome.

where c_L and c_T are the p-wave and s-wave velocities of the medium, respectively. The 0 layer and the N+1 layer satisfy only the scalar wave equation, and any layer of a FGM acoustic window must satisfy the scalar and vector wave equation. A double Fourier transform is applied to Eq. (2) to obtain the general solution form of the velocity potential of each layer in the wavenumber-frequency space:

$$\begin{cases} \widetilde{\phi}_l(k,\omega,z) = A_l e^{-i\sqrt{k_{Ll}^2-k^2}z} + B_l e^{i\sqrt{k_{Ll}^2-k^2}z}, \\ \widetilde{\psi}_l(k,\omega,z) = C_l e^{-i\sqrt{k_{Tl}^2-k^2}z} + D_l e^{i\sqrt{k_{Tl}^2-k^2}z}, \end{cases} \tag{3}$$

where l is any intermediate layer of an FGM acoustic window, k_{Ll} and k_{Tl} are the wavenumbers of the corresponding longitudinal wave and shear wave, respectively; A_l, B_l, C_l, and D_l are the general solution coefficients. Then, the general solution in layer 0 is $\widetilde{\phi}_0(k,\omega,z) = A_0 e^{-i\sqrt{k_{L0}^2-k^2}z}$. The general solution in layer N+1 needs to satisfy the reflection coefficient of the sonar array surface:

$$R = \frac{A_{N+1}e^{-i\sqrt{k_{LN+1}^2-k^2}L}}{B_{N+1}e^{i\sqrt{k_{LN+1}^2-k^2}L}}, \tag{4}$$

then

$$\widetilde{\phi}_{N+1}(k,z) = A_{N+1}\left(e^{i\sqrt{k_{LN+1}^2-k^2}(z-h)} + \mathrm{Re}^{2i\sqrt{k_{LN+1}^2-k^2}L}e^{-i\sqrt{k_{LN+1}^2-k^2}(z-h)}\right)$$

is the general solution in layer N+1.

Here, k_{L0} and k_{LN+1} represent the wavenumbers of the longitudinal wave in layer 0 and layer N+1, respectively. According to the transfer matrix idea (Skelton, James, 1997; Brekhovskikh, 2012), for any intermediate layer l:

$$\begin{bmatrix} \widetilde{V}_x^l \\ \widetilde{V}_z^l \\ \sigma_{zz}^l \\ \sigma_{zx}^l \end{bmatrix} = \mathbf{I}\,|z = z_{lT} \begin{bmatrix} A_l + B_l \\ A_l - B_l \\ C_l - D_l \\ C_l + D_l \end{bmatrix}, \quad \begin{bmatrix} \widetilde{V}_x^{l-1} \\ \widetilde{V}_z^{l-1} \\ \sigma_{zz}^{l-1} \\ \sigma_{zx}^{l-1} \end{bmatrix} = \mathbf{I}\,|z = z_{lB} \begin{bmatrix} A_l + B_l \\ A_l - B_l \\ C_l - D_l \\ C_l + D_l \end{bmatrix}, \tag{5}$$

where $\widetilde{V}_x^l$, $\widetilde{V}_z^l$, σ_{zz}^l, σ_{zx}^l and $\widetilde{V}_x^{l-1}$, $\widetilde{V}_z^{l-1}$, σ_{zz}^{l-1}, σ_{zx}^{l-1} are the results of the double Fourier transforms of the velocity and stress components of the upper interface ($z = z_{lt}$) and the lower interface ($z = z_{lb}$) of the l layer, respectively. The appendix describes the construction of matrix $\mathbf{I}$. The boundary region of the elastic medium satisfies the continuous conditions of the velocity and stress. Then, the relationship between the physical quantity of the lower interface of the N-th layer ($z = z_N$) and the upper interface of the first layer ($z = 0$) is as follows:

$$\begin{bmatrix} \widetilde{V}_x^N \\ \widetilde{V}_z^N \\ \sigma_{zz}^N \\ \sigma_{zx}^N \end{bmatrix} = T_N T_{N-1} \ldots T_1 \begin{bmatrix} \widetilde{V}_x^0 \\ \widetilde{V}_z^0 \\ \sigma_{zz}^0 \\ \sigma_{zx}^0 \end{bmatrix} = F \begin{bmatrix} \widetilde{V}_x^0 \\ \widetilde{V}_z^0 \\ \sigma_{zz}^0 \\ \sigma_{zx}^0 \end{bmatrix}, \tag{6}$$

where $T_l = \mathbf{I}\,|z = z_{lt}\,\mathbf{I}^{-1}\,|z = z_{lb}$ and $F = T_N T_{N-1} \ldots T_1$.

The conditions of the velocity and stress continuity are satisfied on the inner and outer boundaries of the acoustic window. After performing the double Fourier transform, the following conditions are satisfied:

$$\begin{cases} z = 0: & -i\rho_0\omega\widetilde{\phi}_0 + \widetilde{F}(k,\omega,z) = \widetilde{\sigma}_{zz}^0, \\ & -\left.\dfrac{\partial\widetilde{\phi}_0}{\partial z}\right|_{z=0} = \widetilde{V}_z^0, \qquad \widetilde{\sigma}_{zx}^0 = 0, \\ z = h: & -i\rho_{N+1}\omega\widetilde{\phi}_{N+1} = \widetilde{\sigma}_{zz}^n, \\ & -\left.\dfrac{\partial\widetilde{\phi}_{N+1}}{\partial z}\right|_{z=h} = \widetilde{V}_z^N, \qquad \widetilde{\sigma}_{zx}^N = 0. \end{cases} \tag{7}$$

Through the six continuous conditions of Eq. (7) and transfer matrix Eq. (6), the unknown coefficients A_0 and A_{N+1} of the acoustic field inside and outside the acoustic window are obtained. The acoustic field outside and inside the acoustic window can be expressed as:

$$\begin{cases} \widetilde{p}_0 = -i\rho_0\omega\widetilde{\phi}_0 = -i\rho_0\omega A_0 e^{-i\sqrt{k_0^2-k^2}z}, \\ \widetilde{p}_{N+1} = -i\rho_{N+1}\omega\widetilde{\phi}_{N+1} \\ \qquad = -iA_{N+1}\rho_{N+1}\omega e^{i\sqrt{k_{N+1}^2-k^2}(z-h)} \\ \qquad\quad \cdot\left(1 + \mathrm{Re}^{2i\sqrt{k_{N+1}^2-k^2}[L-2(z-h)]}\right), \end{cases} \tag{8}$$

where $k_0 = \frac{\omega}{c_0}$, $k_{N+1} = \frac{\omega}{c_{N+1}}$ and ρ_0, c_0, ρ_{N+1}, and c_{N+1} are the density and acoustic velocity of the 0-th and (N+1)-th layers, respectively. Then, A_0 and A_{N+1} are:

$$\begin{aligned} A_0 &= i\frac{(C_{23} - PC_{33})\widetilde{F}(k,\omega,z)}{\sqrt{k_0^2-k^2}(C_{22} - PC_{32}) + \rho_0\omega(C_{23} - PC_{33})}, \\ A_{N+1} &= \frac{\sqrt{k_0^2-k^2}C_{32}A_0 + C_{33}\left(\rho_0\omega A_0 - i\widetilde{F}(k,\omega,z)\right)}{\rho_{n+1}\omega\left(1 + \mathrm{Re}^{2i\sqrt{k_{N+1}^2-k^2}l}\right)}, \end{aligned} \tag{9}$$

where

$$\begin{cases} P = -\dfrac{\sqrt{k_{N+1}^2-k^2}\left(1-\mathrm{Re}^{2i\sqrt{k_{N+1}^2-k^2}l}\right)}{\rho_{N+1}\omega\left(1+\mathrm{Re}^{2i\sqrt{k_{N+1}^2-k^2}l}\right)}, \\ C_{ij} = F_{ij} - \dfrac{F_{4j}F_{i1}}{F_{41}}. \end{cases} \tag{10}$$

According to Eq. (5), the acoustic pressure on the surface of the sonar array can be obtained at $z = h + L$. Then, the spatial filter function of the acoustic window $G(k,\omega)$ can be expressed as:

$$G(k,\omega) = -i\rho_{N+1}\omega\widetilde{\phi}_{N+1}\,|z = h + L. \tag{11}$$

Furthermore, the wavenumber-frequency spectrum of the TBL pulsating pressure needs to be obtained as the excitation source for evaluating the vibration-acoustic response of the structure. The Corcos model (Caiazzo, Desmet, 2016; Tang *et al.*, 2020), the earliest and most widely used model of the TBL pulsating pressure, is adopted in this paper. The model reflects the migration characteristics of the TBL pulsating pressure. The cross-spectrum density can be obtained by integrating the Fourier transform:

$$\Phi_{ff}(k,\omega) = \frac{\Phi_{ff}(\omega)}{\pi^2}\frac{\alpha_1\alpha_3\omega^2}{U_c^2} \cdot \frac{1}{\left(\left(k_1 - \frac{\omega}{U_c}\right)^2 + \left(\alpha_1\frac{\omega}{U_c}\right)^2\right)\left(k_3^2 + \left(\alpha_3\frac{\omega}{U_c}\right)^2\right)}, \tag{12}$$

where $\alpha_1 = 0.09$, $\alpha_3 = 7\alpha_1$, and $U_c = 0.6U$.

Therefore, the wavenumber-frequency spectrum density function of the sonar array surface under the TBL pulsating pressure excitation can be obtained as:

$$\Phi_{pp}(\omega) = \int_{-\infty}^{\infty}\Phi_{ff}(k,\omega)\,|G(k,\omega)|^2\,\mathrm{d}k, \tag{13}$$

where $\Phi_{ff}(k,\omega)$ is the wavenumber-frequency spectrum of the TBL pulsating pressure and $G(k,\omega)$ is the spatial filter function of the sonar dome.

The frequency spectrum density function of the TBL pulsating pressure in the absence of an acoustic window is:

$$\Phi_{pp}^0(\omega) = \int_{-\infty}^{\infty}\Phi_{ff}(k,\omega)\,\mathrm{d}k. \tag{14}$$

The turbulent self-noise reduction of an acoustic window can be defined as:

$$\mathrm{NR} = 10\log\frac{\Phi_{pp}(\omega)}{\Phi_{pp}^0(\omega)}. \tag{15}$$

The turbulent self-noise suppression effect of two kinds of acoustic windows is defined as the difference in the turbulent self-noise reduction:

$$\mathrm{NR}' = \mathrm{NR}_1 - \mathrm{NR}_2. \tag{16}$$

2.2. Theoretical model of the STL for the sonar dome under plane wave excitation

With the plane wave as the excitation source, the sound field outside the FGM acoustic window is the sum of the incident velocity potential function ϕ_i and the reflection potential function ϕ_r. The sound field outside the acoustic window obtained by the double Fourier transform is:

$$\begin{aligned}\widetilde{\phi}_0(k,\omega,z) &= \widetilde{\phi}_i(k,\omega,z) + \widetilde{\phi}_r(k,\omega,z)\\ &= e^{i\sqrt{k_0^2-k^2}z} + a_0 e^{-i\sqrt{k_0^2-k^2}z},\end{aligned} \tag{17}$$

where $k_0 = \frac{\omega}{c_0}$ and $k = k_0\sin\theta$ with incident angle θ. The acoustic field inside the sonar cavity excited by the incident plane wave is similar to:

$$\widetilde{\phi}_{n+1}(k,\omega,z) = a_{N+1}\left(e^{i\sqrt{k_{N+1}^2-k^2}(z-h)} + \mathrm{Re}^{2i\sqrt{k_{N+1}^2-k^2}l}e^{-i\sqrt{k_{N+1}^2-k^2}(z-h)}\right). \tag{18}$$

The general solutions of the scalar potential function and vector potential function of the intermediate elastic gradient material are consistent with Eq. (3), similar to the matrix transfer relation. Combined with boundary conditions, the following is obtained:

$$\begin{cases} z = 0: & -i\rho_0\omega\widetilde{\phi}_0 = \widetilde{\sigma}_{zz}^0,\\ & -\left.\dfrac{\partial\widetilde{\phi}_0}{\partial z}\right|_{z=0} = \widetilde{V}_z^0, \qquad \widetilde{\sigma}_{zx}^0 = 0,\\ z = h: & -i\rho_0\omega\widetilde{\phi}_{n+1} = \widetilde{\sigma}_{zz}^n,\\ & -\left.\dfrac{\partial\widetilde{\phi}_{n+1}}{\partial z}\right|_{z=h} = \widetilde{V}_z^n, \qquad \widetilde{\sigma}_{zx}^n = 0. \end{cases} \tag{19}$$

With the redundant components eliminated, the acoustic field inside and outside the acoustic window can be expressed as:

$$\begin{cases} \widetilde{p}_0 = -i\rho_0\omega\widetilde{\phi}_0 = -i\rho_0\omega\left(e^{i\sqrt{k_0^2-k^2}z} + a_0 e^{-i\sqrt{k_0^2-k^2}z}\right),\\ \widetilde{p}_{n+1} = -i\rho_{N+1}\omega\widetilde{\phi}_{n+1}\\ \qquad = -ia_{N+1}\rho_0\omega\left(e^{i\sqrt{k_{N+1}^2-k^2}(z-h)} + \mathrm{Re}^{2i\sqrt{k_{N+1}^2-k^2}L}e^{-i\sqrt{k_{N+1}^2-k^2}(z-h)}\right), \end{cases} \tag{20}$$

where a_0 and a_{N+1} are given as:

$$\begin{aligned} a_0 &= \frac{\sqrt{k_0^2-k^2}\,(C_{22}-pC_{32}) - \rho_0\omega\,(C_{23}-pC_{33})}{\sqrt{k_0^2-k^2}\,(C_{22}-pC_{32}) + \rho_0\omega\,(C_{23}-pC_{33})},\\ a_{N+1} &= \frac{\sqrt{k_0^2-k^2}C_{32}\,(1-a_0) + \rho_0\omega C_{33}\,(1+a_0)}{\rho_{n+1}\omega\left(1+\mathrm{Re}^{2i\sqrt{k_{N+1}^2-k^2}L}\right)}. \end{aligned} \tag{21}$$

The matrix $\mathbf{C}$ is consistent with Eq. (10), and

$$p = -\frac{\sqrt{k_{N+1}^2-k^2}\left(1-\mathrm{Re}^{2i\sqrt{k_{N+1}^2-k^2}L}\right)}{\rho_{n+1}\omega\left(1+\mathrm{Re}^{2i\sqrt{k_{N+1}^2-k^2}L}\right)}. \tag{22}$$

To evaluate the sound transmission performance of FGM acoustic windows, the STL (insertion loss) should be calculated. When acoustic windows do not exist, the acoustic pressure at the $z = h$ position should be:

$$\widetilde{p}'_{N+1} = -i\omega\rho_0 \left(e^{i\sqrt{k_{N+1}^2 - k^2}h} + \mathrm{Re}^{i\sqrt{k_{N+1}^2 - k^2}(h+2L)} \right). \quad (23)$$

The STL is:

$$\mathrm{STL} = -20\log\left(\left| \frac{\widetilde{p}_{N+1}}{\widetilde{p}'_{N+1}} \right| \right). \quad (24)$$

2.3. Verification of the theoretical model of the wave-frequency response function of the turbulent self-noise and STL for FGM acoustic windows

The turbulent self-noise caused by the TBL pulsating pressure can be simplified to the acoustic field in the sonar cavity with the acoustic window excited by a point force. The STL of the acoustic window under the plane wave excitation is calculated in the usual way. A linear FRP-rubber FGM acoustic window with $N = 50$ is selected to verify the theoretical results. The material properties setting of every layer are shown in Eq. (28). The material parameters of the FRP and rubber are shown in Table 2.

In Fig. 2, the depth of the sonar cavity is 0.5 m, and the reflection coefficient of the sonar array surface is 0.3. The thickness of the perfectly matched layer (PML) is 0.1 m, and H_1, H_2, L_1, and L_2 are 0.5, 0.3, 100, and 0.5 m, respectively. The theoretical and simulation results of the STL of the linear FRP-rubber FGM acoustic window are shown in Fig. 3.

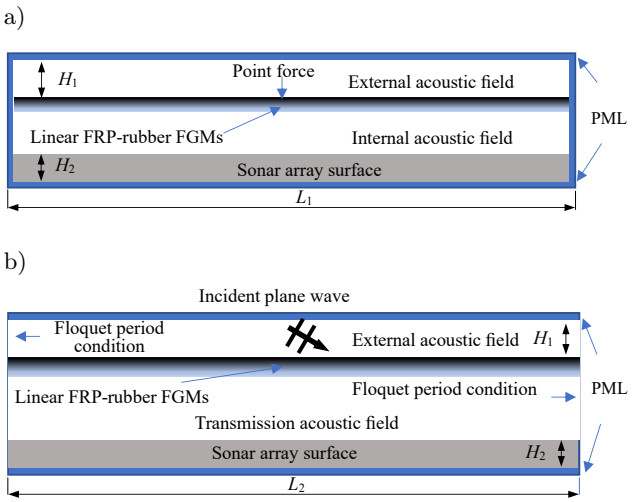

Fig. 2. Calculation setting of the linear FRP-rubber FGM acoustic window in COMSOL Multiphysics software: a) wave-frequency response function; b) STL.

For the acoustic field in the sonar cavity with the linear FRP-rubber FGM acoustic window excited by a point force, the wavenumber-frequency spectrum results of the acoustic pressure on the sonar array surface are selected for comparison, which is shown in Fig. 4.

The results in Figs. 3 and 4 show that the simulation and theoretical results are in complete agreement, both in the calculation results of the STL and in the wavenumber-frequency spectrum results of the acoustic field in the sonar cavity for the linear FRP-rubber FGM acoustic window. Therefore, the accuracy of the theoretical model of the wavenumber frequency response function of the turbulent self-noise and STL are verified for the sonar dome.

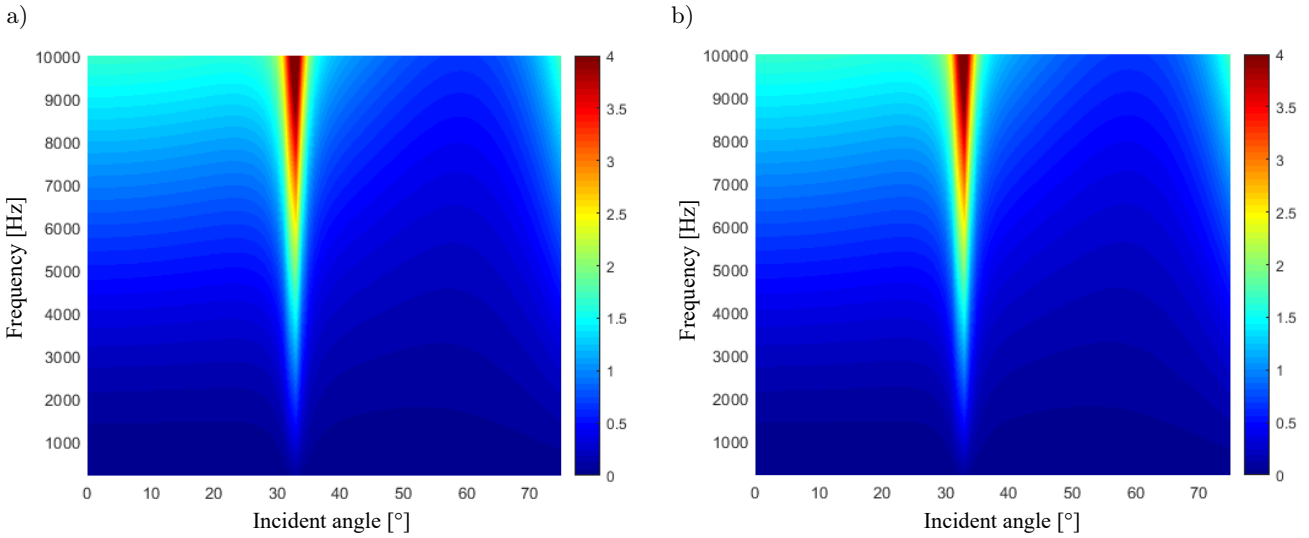

Fig. 3. Comparison results of the STL of the linear FRP-rubber FGM acoustic window: a) theoretical result; b) simulation result.

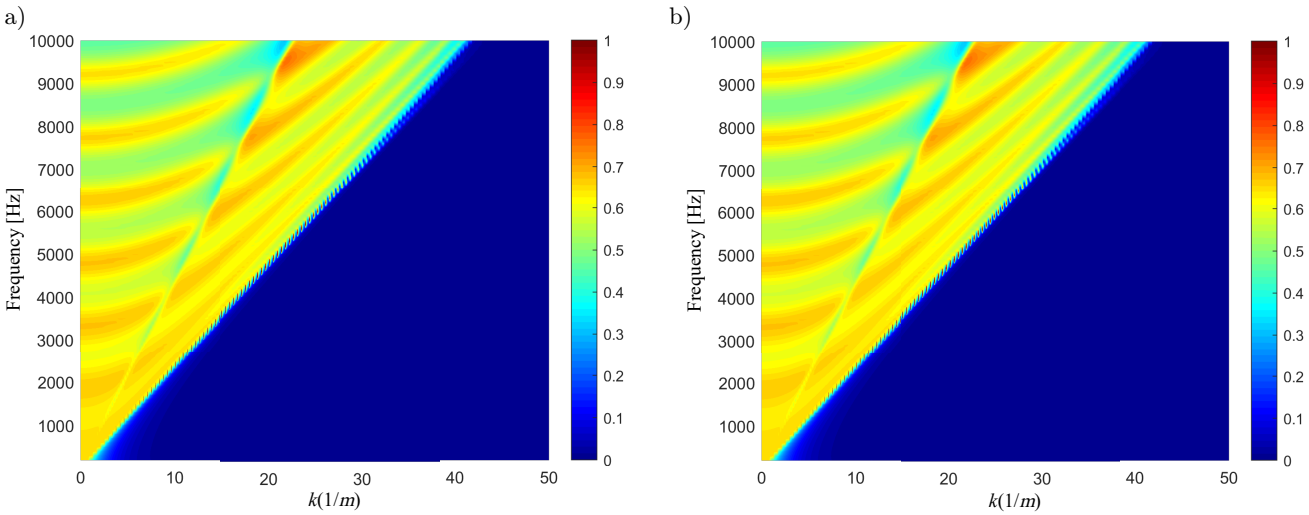

Fig. 4. Comparison results of the wavenumber-frequency spectrum of the acoustic pressure on the sonar array surface in the sonar cavity: a) theoretical result; b) simulation result.

3. Internal gradient optimization design for FGM acoustic windows based on turbulent self-noise suppression and the sound transmission performance

The material properties of FGM are mainly determined by the substrate, top material and an internal gradient form. Different forms of the internal gradients result in different material properties. Therefore, by studying the internal gradient of the FGM, an optimization method of internal gradients that can design an optimized FGM acoustic window with better turbulent self-noise suppression and sound transmission performance is proposed in this paper (Fig. 5). The existing gradient design mainly includes parabolic functions, power-law functions and exponential functions, but none of them offer a favorable

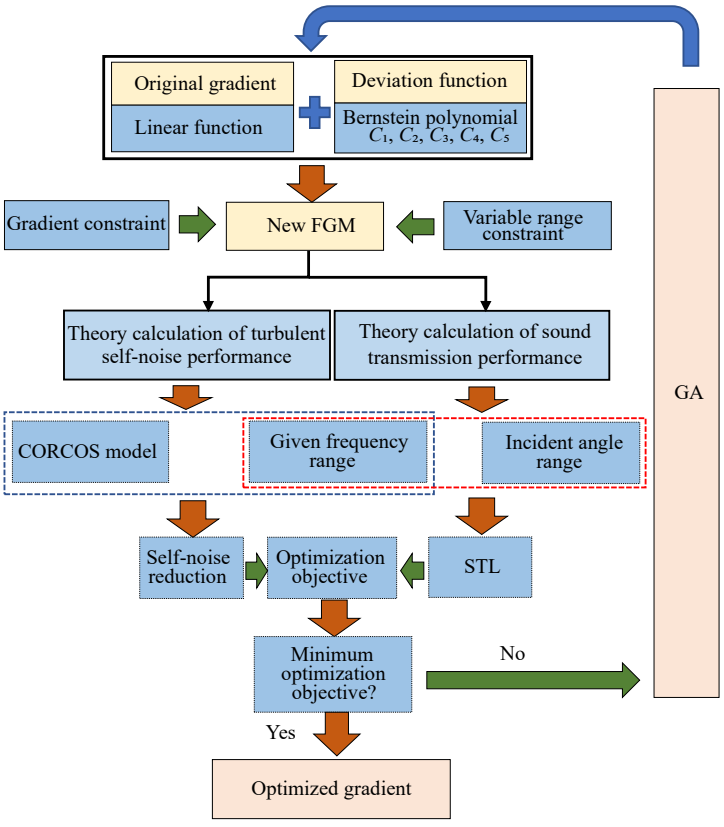

Fig. 5. Overall flow chart of the gradient optimization design method.

function change space. Therefore, in the optimization method, the space layout of the gradient change is readjusted by introducing a deviation function term expressed by the Bernstein polynomial on the basis of the original linear gradient. In addition, upon combining the GA and taking the monotonic gradient as the constraint condition, the results of five optimization variables carried by the Bernstein polynomial when the optimization objective is minimized are obtained in the optimization method by iterating the gradient function. The optimization objective is expressed as the STL, the turbulent self-noise reduction or a weighting function of the STL and turbulent self-noise reduction of FGM acoustic windows.

3.1. Internal gradient function design of FGM acoustic windows

The existing internal gradient change functions of FGMs mainly include parabolic, power-law and exponential functions. These functions have a small adjustment range for the gradient change space, and only convex or concave functions can be selected, which limits the gradient change. Therefore, a deviation function expressed by the Bernstein polynomial is introduced on the basis of the original linear gradient function. By adjusting different parameters in the Bernstein polynomials, the overall coverage of the space range of the optimized gradient is achieved to seek the overall optimal solution (Fig. 6).

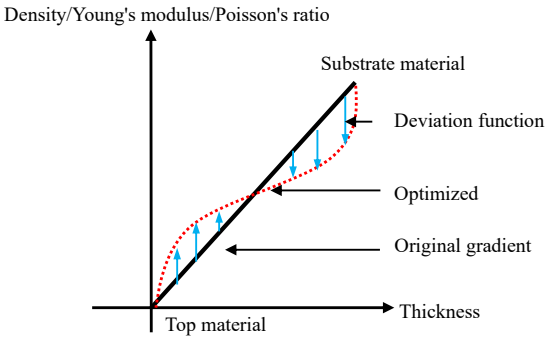

Fig. 6. Optimization gradient design schematic.

The deviation function expressed by the Bernstein polynomial is shown in Eq. (25):

$$\Delta z = \sum_{i=0}^{M} C_i s^i * (1-s)^{(M-i)}. \tag{25}$$

The optimization results often depend on the order of the Bernstein polynomials. The more orders that are selected, the finer and better the results that may be obtained. However, the time required for the optimization calculation increases exponentially. Moreover, unsatisfactory optimization results become more likely. Therefore, $M = 5$ is selected to obtain better optimization results. The boundary of $i = 0$ is omitted, ensuring that the properties of the substrate material and the top material remain unchanged in the optimization process. The deviation function is shown in Eq. (26):

$$\Delta E = (E_t - E_b) \sum_{i=1}^{5} C_i \left(\frac{h}{H}\right)^i \left(1 - \frac{h}{H}\right)^{(5-i)}. \tag{26}$$

The gradient function is shown as:

$$E = \frac{E_t - E_b}{H} h + E_b + \Delta E. \tag{27}$$

The specific gradient functions of the density, Young's modulus and Poisson's ratio are:

$$\begin{cases} \rho = \dfrac{\rho_t - \rho_b}{H} h + \rho_b \\ \quad + (\rho_t - \rho_b) \displaystyle\sum_{i=1}^{5} C_i \left(\frac{h}{H}\right)^i \left(1 - \frac{h}{H}\right)^{(5-i)}, \\ E = \dfrac{E_t - E_b}{H} h + E_b \\ \quad + (E_t - E_b) \displaystyle\sum_{i=1}^{5} C_i \left(\frac{h}{H}\right)^i \left(1 - \frac{h}{H}\right)^{(5-i)}, \\ \sigma = \dfrac{\sigma_t - \sigma_b}{H} h + \sigma_b \\ \quad + (\sigma_t - \sigma_b) \displaystyle\sum_{i=1}^{5} C_i \left(\frac{h}{H}\right)^i \left(1 - \frac{h}{H}\right)^{(5-i)}. \end{cases} \tag{28}$$

3.2. Optimization algorithm, constraints and variable range

To obtain the global optimal solution, a GA is used in this paper. The GA is a kind of stochastic global search and optimization method that simulates the natural selection and genetic mechanism of Darwin evolution. The GA is essentially an efficient, parallel, and global searching method, that can automatically acquire and accumulate information about the search space and adaptive control of the search process to obtain the best solution (Fig. 7). When enough initial random samples are satisfied, the globally unique optimal solution can be obtained.

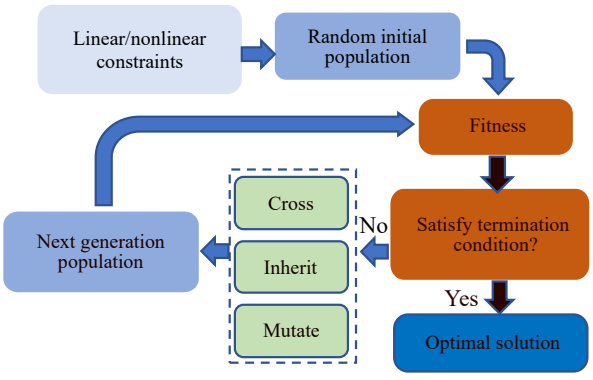

Fig. 7. Optimization flow of the GA.

The termination conditions include population genetic algebra and tolerance. Most of the existing FGMs meet the monotonic variation trend. Therefore, a nonlinear gradient constraint is applied to the GA:

$$\frac{\mathrm{d}E}{\mathrm{d}h} \geq 0. \tag{29}$$

According to Eq. (28), the gradient function in the optimization process is regulated by five optimization variables. Table 1 shows the initial value and variation range of each optimization variable.

Table 1. Range setting of the optimization variables in the gradient function.

Optimization variables	Initial value	Minimum value	Maximum value
C_1	0	−25	25
C_2	0	−25	25
C_3	0	−25	25
C_4	0	−25	25
C_5	0	−25	25

3.3. Optimization objective function

The design of FGM acoustic windows should not only consider the effect of turbulent self-noise suppression in sonar cavities but also meet the requirement of sound transmission performance. Therefore, the optimization objective function should be designed considering turbulent self-noise reduction and STL at the same time. In the engineering design of sonar acoustic windows, the STL in the incident angle range of 0–75° should be as small as possible, and the turbulent self-noise reduction should be as high as possible. Therefore, the objective function of optimization is shown as:

$$\begin{cases} F_1 = 10\log\left(\sum\limits_{\theta=\theta_i}^{\theta_j}\sum\limits_{f=f_i}^{f_j} 10^{\mathrm{TL}(f,\theta)}\right), \\ \qquad \sum\limits_{f=f_i}^{f_j}(\mathrm{NR}(f)) = C, \\ F_2 = \sum\limits_{f=f_i}^{f_j}(\mathrm{NR}(f)), \\ \qquad 10\log\left(\sum\limits_{\theta=\theta_i}^{\theta_j}\sum\limits_{f=f_i}^{f_j} 10^{\mathrm{TL}(f,\theta)}\right) = C, \\ F_3 = \dfrac{10\log\left(\sum\limits_{\theta=\theta_i}^{\theta_j}\sum\limits_{f=f_i}^{f_j} 10^{\mathrm{TL}(f,\theta)}\right)}{\sum\limits_{f=f_i}^{f_j}(\mathrm{NR}(f))}, \end{cases} \tag{30}$$

where f_i is the initial frequency, f_j is the termination frequency, θ_i is the initial optimization angle, θ_j is the end angle, and C is a constant; TL is the transmission loss in the optimal frequency range $(f_i - f_j)$ and angle range $(\theta_i - \theta_j)$; F_i $(i = 1, 2, 3)$ is the objective function of the optimization. F_1 and F_2 can achieve the optimal sound transmission performance or turbulent self-noise suppression performance for FGM acoustic windows, respectively, when the turbulent self-noise suppression performance or sound transmission performance remains unchanged. The minimum optimization objective function F_3 can achieve the effect of the maximum turbulent self-noise reduction and minimum the STL for FGM acoustic windows.

4. Optimization results of the internal gradient of FGM acoustic windows

According to the designed internal gradient optimization method of FGM acoustic windows, the existing FRP-rubber FGM acoustic window is optimized. The materials and properties involved are shown in Table 2.

Here, the optimization results of the internal gradient design for the FRP-rubber FGM acoustic window are presented with $H = 3$ cm, $L = 0.5$ m, and $R = 0.3$.

Moreover, the theoretical model of the turbulent self-noise suppression and sound transmission characteristics of the sonar dome proposed in this paper is solved by discretizing the continuous medium into a layered medium of the acoustic window. Differences in layering affect the calculation accuracy of the theoretical results. Figure 8 shows the layered N convergence calculation results with respect to the turbulent self-noise reduction and STL of the linear FRP-rubber FGM. With increasing N, these parameters gradually converge. To ensure the calculation efficiency and accuracy, the ratio of the corresponding wavelength to the thickness of a single layer is selected to be above 250, corresponding to $N = 50$ at $f = 10$ kHz.

4.1. Optimization of sound transmission performance with turbulent self-noise suppression performance unchanged

According to the optimization method proposed in this paper, the STL of the FRP-rubber FGM acoustic window is taken as the optimization objective function to carry out the calculation when the turbulent self-noise reduction remains unchanged, as shown

Table 2. Materials and properties.

Material	Density [kg/m^3]	Young's modulus [N/m^2]	Poisson's ratio	Longitudinal wave velocity [m/s]	Shear wave velocity [m/s]	Loss factor
FRP	1620	1.74e10	0.2	3455	2116	0.03
Rubber	1030	1.67e9	0.33	1550	781	0.3

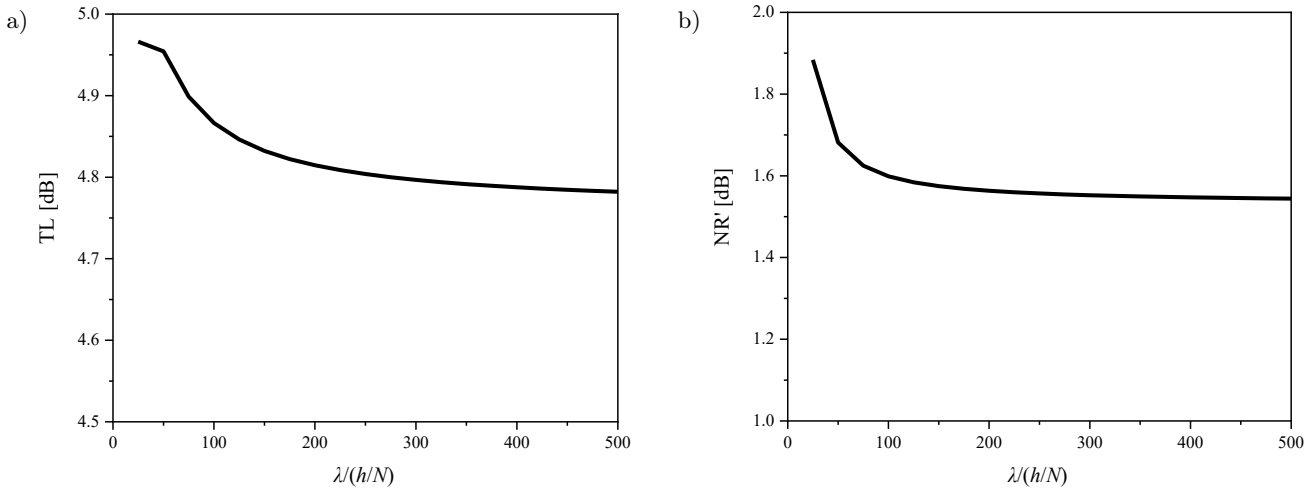

Fig. 8. Convergence relationship with the wavelength to monolayer thickness ratio: a) STL; b) turbulent self-noise reduction.

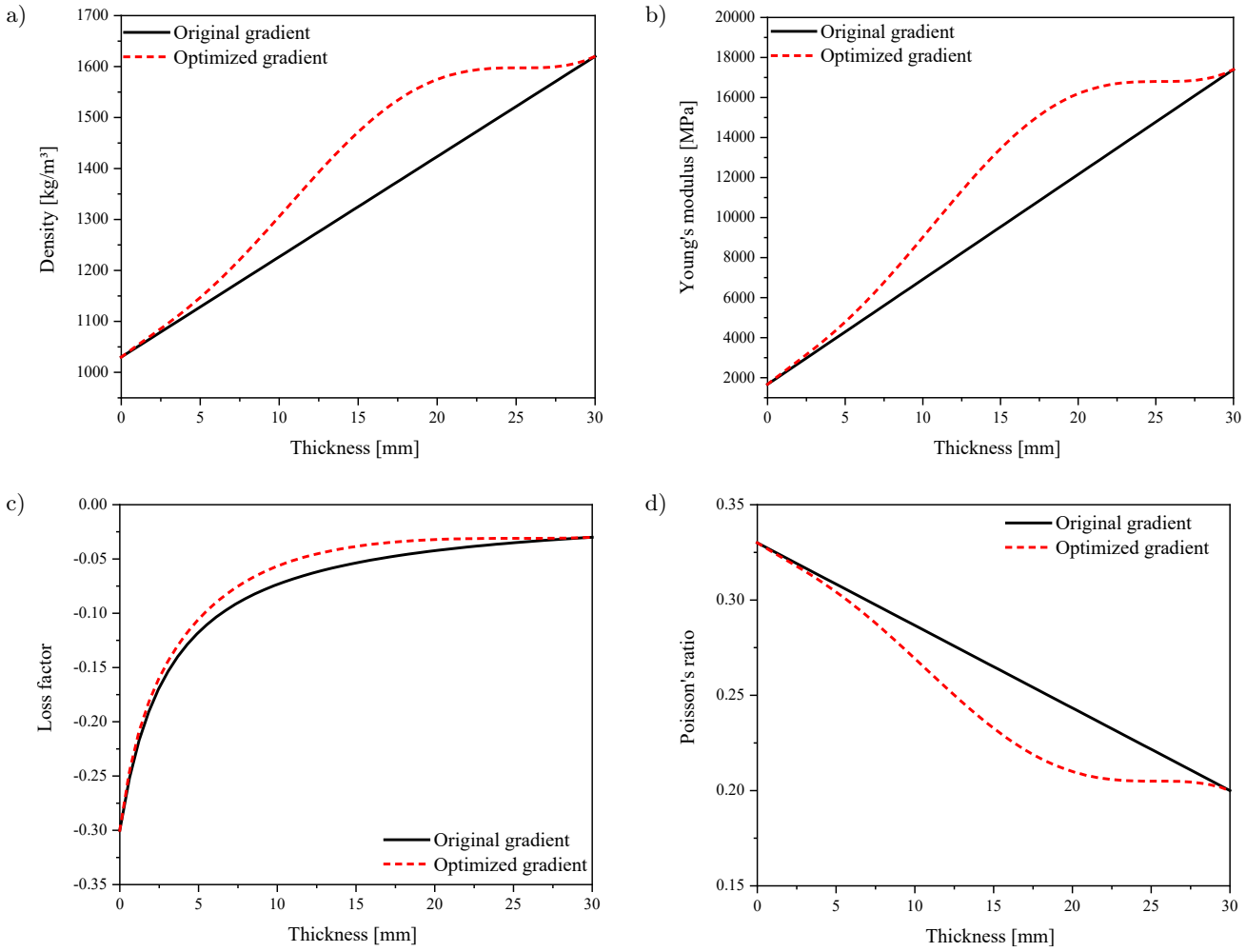

Fig. 9. Comparison results of the FRP-rubber FGM acoustic window before and after the sound transmission performance optimization: a) density; b) Young's modulus; c) loss factor; d) Poisson's ratio.

in Eq. $(30)_1$. The incident angle range of the STL optimization is selected to be 0–75° with a step size of 1°. The optimization frequency range of the STL and turbulent self-noise is selected to be 0.2–10 kHz with a step of 0.1 kHz. The main frequency of the calculation computer is 4.5 GHz, the memory is 64 GB,

and the total optimization computing time is 3.45 days. The optimized parameters are shown in Table 3.

Table 3. Calculation results of the gradient optimization variables of the FRP-rubber FGM acoustic window with sound transmission performance optimization.

Optimization variables	C_1	C_2	C_3	C_4	C_5
Optimization results	0.2345	6.4928	9.8355	−0.8583	0.1961

The comparison results of the density, Young's modulus, the loss factor, and Poisson's ratio of the FRP-rubber FGM acoustic window before and after the sound transmission performance optimization are shown in Fig. 9.

The comparison results of the self-noise suppression and the sound transmission performance of the FRP-rubber FGM acoustic window before and after the sound transmission performance optimization are shown in Fig. 10.

Figure 10 shows that the optimized FGM acoustic window is superior to the initial linear FGM acoustic window in the sound transmission performance when the turbulent self-noise suppression performance remains unchanged. From Fig. 10b, the peak of the STL of the optimized FGM acoustic window compared to that of the initial linear FGM acoustic window decreases by approximately 0.8 dB at $f = 10$ kHz, which corresponds to an 17% increase in the sound transmission performance. Moreover, the optimized effect is not ideal at lower incident angles because the optimization objective function F_1 is the total STL of the optimization angle range without considering every angle optimization effect separately. The value and position changes of the STL peak before and after optimization, and whether it is benefit for the sound transmission performance are explained in Sec. 5.

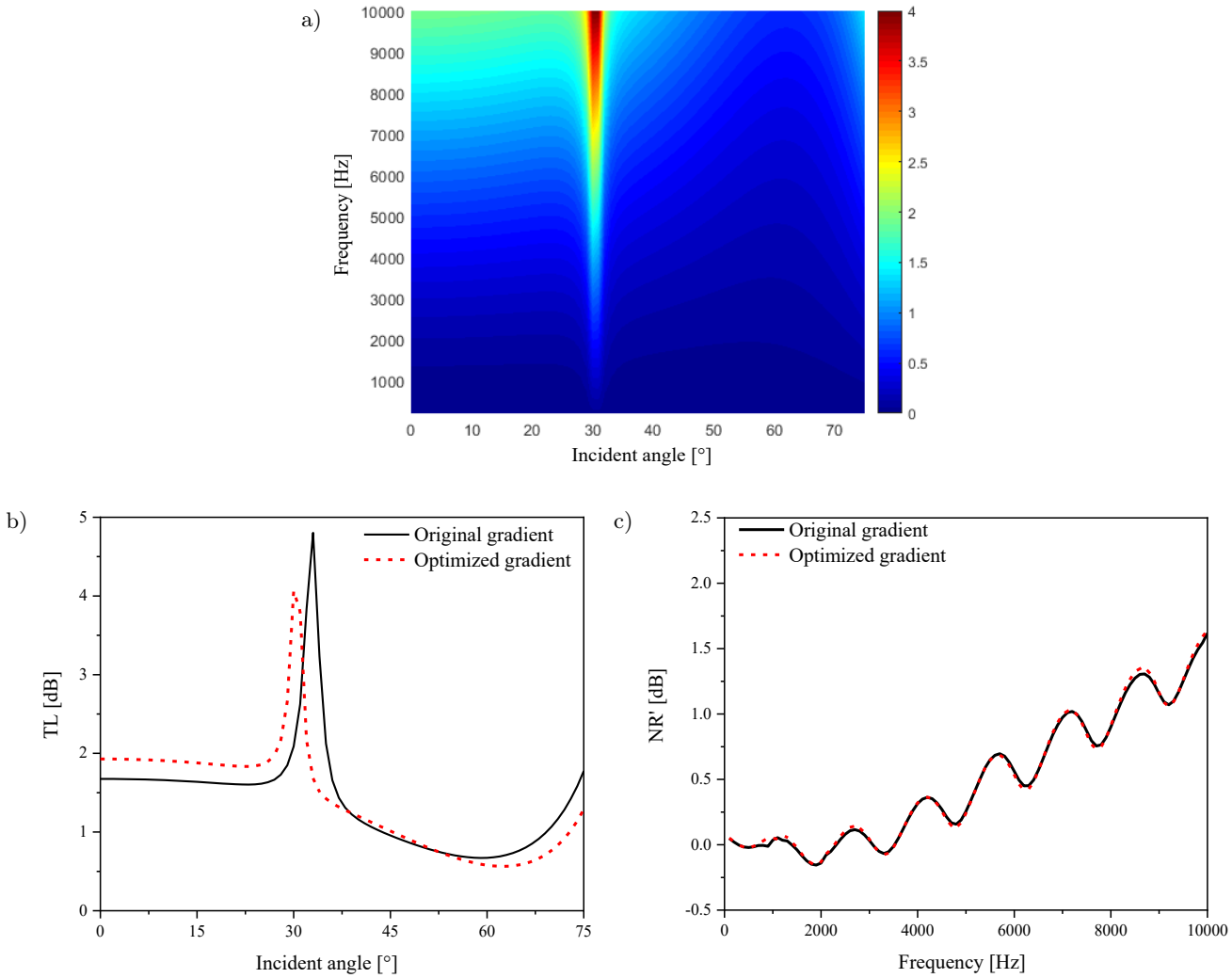

Fig. 10. Comparison results of the turbulent self-noise reduction and STL of the FRP-rubber FGM acoustic window before and after the sound transmission performance optimization: a) STL of the optimized FGM; b) STL at $f = 10$ kHz; c) comparison of the turbulent self-noise reduction.

4.2. Optimization of the turbulent self-noise suppression performance while maintaining the sound transmission performance

According to the optimization method proposed in this paper, the turbulent self-noise reduction of the FRP-rubber FGM acoustic window is taken as the optimization objective function to carry out the calculation when the STL remains unchanged, as shown in Eq. $(30)_2$. The angle and frequency range of the sound transmission performance optimization and the frequency range of the turbulent self-noise suppression optimization are consistent with the above. The computer parameters are consistent with those above, and the total optimization computing time is 3.95 days. The optimized parameters are shown in Table 4.

The comparison results of the density, Young's modulus, the loss factor and Poisson's ratio of the FRP-rubber FGM acoustic window before and after the turbulent self-noise suppression performance optimization are shown in Fig. 11.

The comparison results of the turbulent self-noise suppression and sound transmission performance of the FRP-rubber FGM acoustic window before and after the turbulent self-noise suppression performance optimization are shown in Fig. 12.

Table 4. Calculation results of the gradient optimization variables of the FRP-rubber FGM acoustic window for turbulent self-noise suppression performance optimization.

Optimization variables	C_1	C_2	C_3	C_4	C_5
Optimization results	0.9679	4.4406	0.9231	−5.1370	−0.9862

Figure 12 shows that the optimized FGM acoustic window is superior to the initial linear FGM acoustic window in turbulent self-noise suppression performance when the sound transmission performance remains unchanged. From Fig. 12c, the turbulent self-noise reduction of the optimized FGM acoustic window is significantly higher than that of the initial FGM acoustic window. Moreover, the self-noise reduction gradually increases with increasing frequency, and the highest self-noise reduction is approximately 0.4 dB at f = 10 kHz, which corresponds to a 25% improvement in the turbulent self-noise suppression performance.

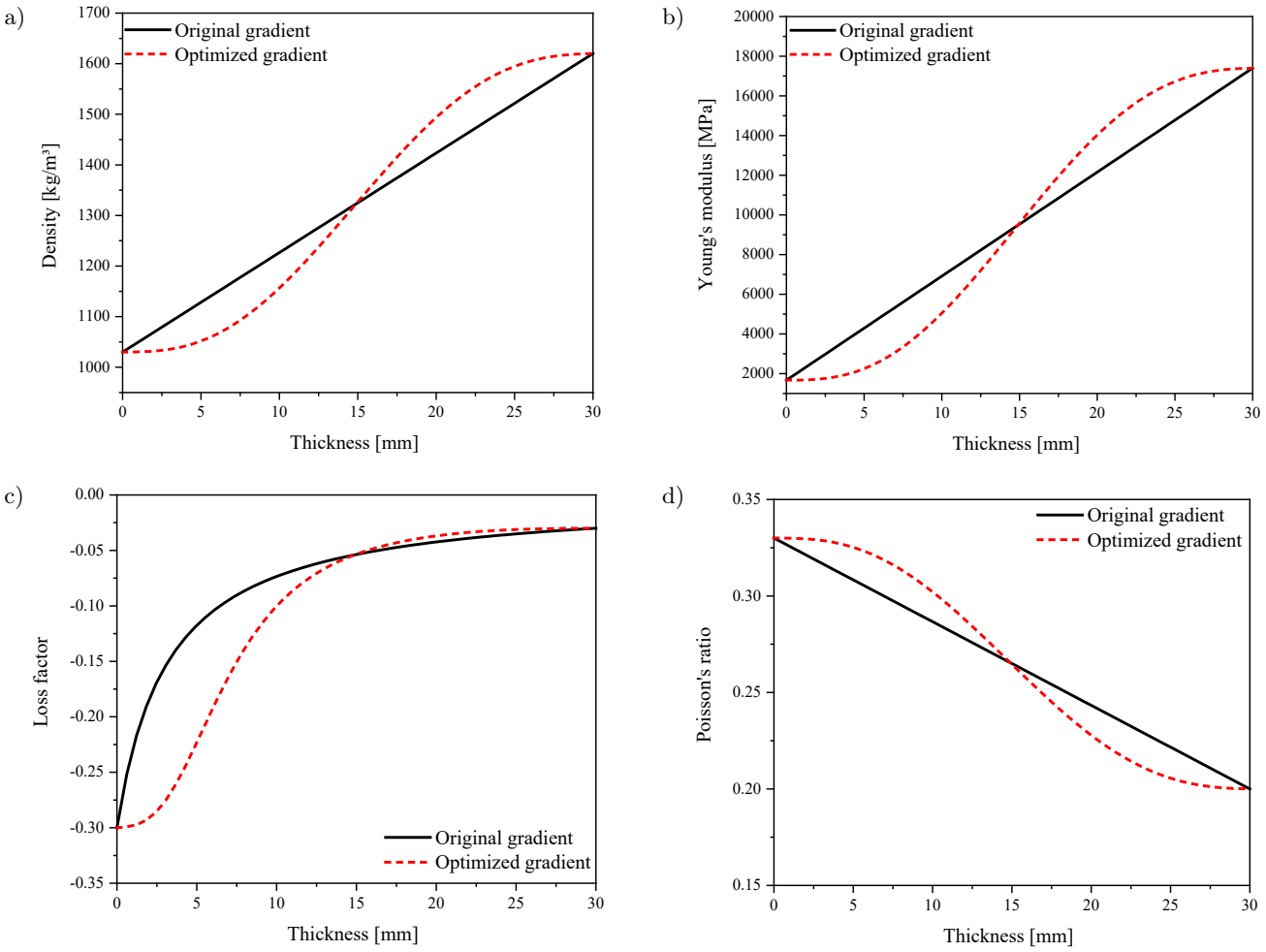

Fig. 11. Comparison results of the FRP-rubber FGM acoustic window before and after the turbulent self-noise suppression performance optimization: a) density; b) Young's modulus; c) loss factor; d) Poisson's ratio.

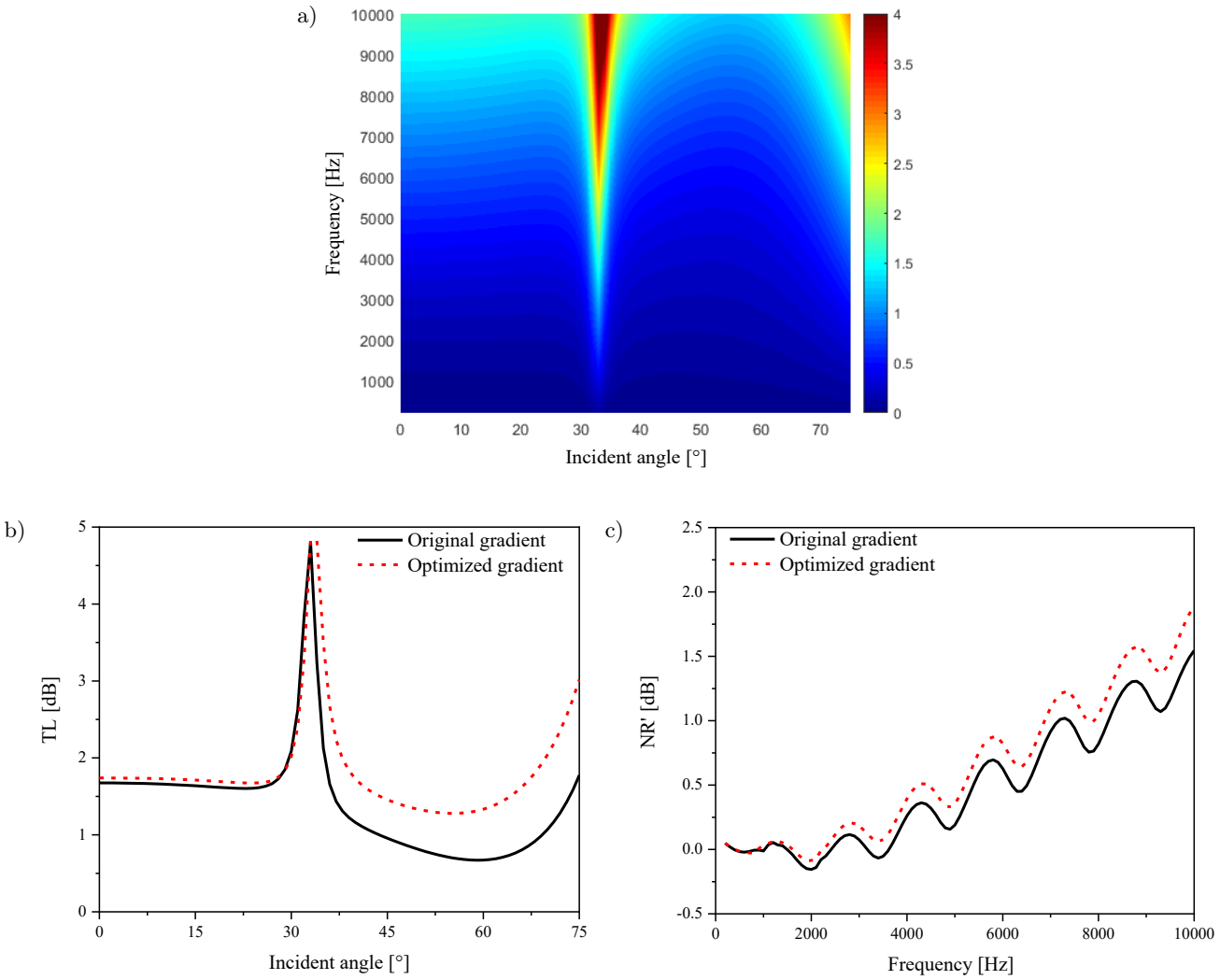

Fig. 12. Comparison results of the turbulent self-noise reduction and STL of the FRP-rubber FGM acoustic window before and after the turbulent self-noise suppression performance optimization: a) STL of the optimized FGM; b) STL at f = 10 kHz; c) comparison of the turbulent self-noise reduction.

In addition, it can also be seen that there is a certain difference for the STL in the higher incident angle range before and after optimization. The reason is that only the total TL is considered in the optimization objective function F_2, which is basically unchanged before and after optimization. The STL at higher incident angles is so small that it makes little contribution to the total STL, which is ignored by the optimization method.

4.3. Optimization of turbulent self-noise suppression and sound transmission performance

According to the optimization method proposed in this paper, the turbulent self-noise reduction and STL of the FRP-rubber FGM acoustic window are taken as the optimization objective function to carry out the calculation, as shown in Eq. $(30)_3$. The angle and frequency range of the sound transmission performance optimization and the frequency range of the turbulent self-noise suppression optimization are consistent with the above. The computer parameters are consistent with those above, and the total optimization computing time is 6.75 days. The optimized parameters are shown in Table 5.

Table 5. Calculation results of the gradient optimization variables of the FRP-rubber FGM acoustic window with turbulent self-noise suppression and sound transmission performance.

Optimization variables	C_1	C_2	C_3	C_4	C_5
Optimization results	0.8339	5.0562	12.2603	0.4194	–1.0000

The comparison results of the density, Young's modulus, the loss factor and Poisson's ratio of the FRP-rubber FGM acoustic window before and after optimization are shown in Fig. 13.

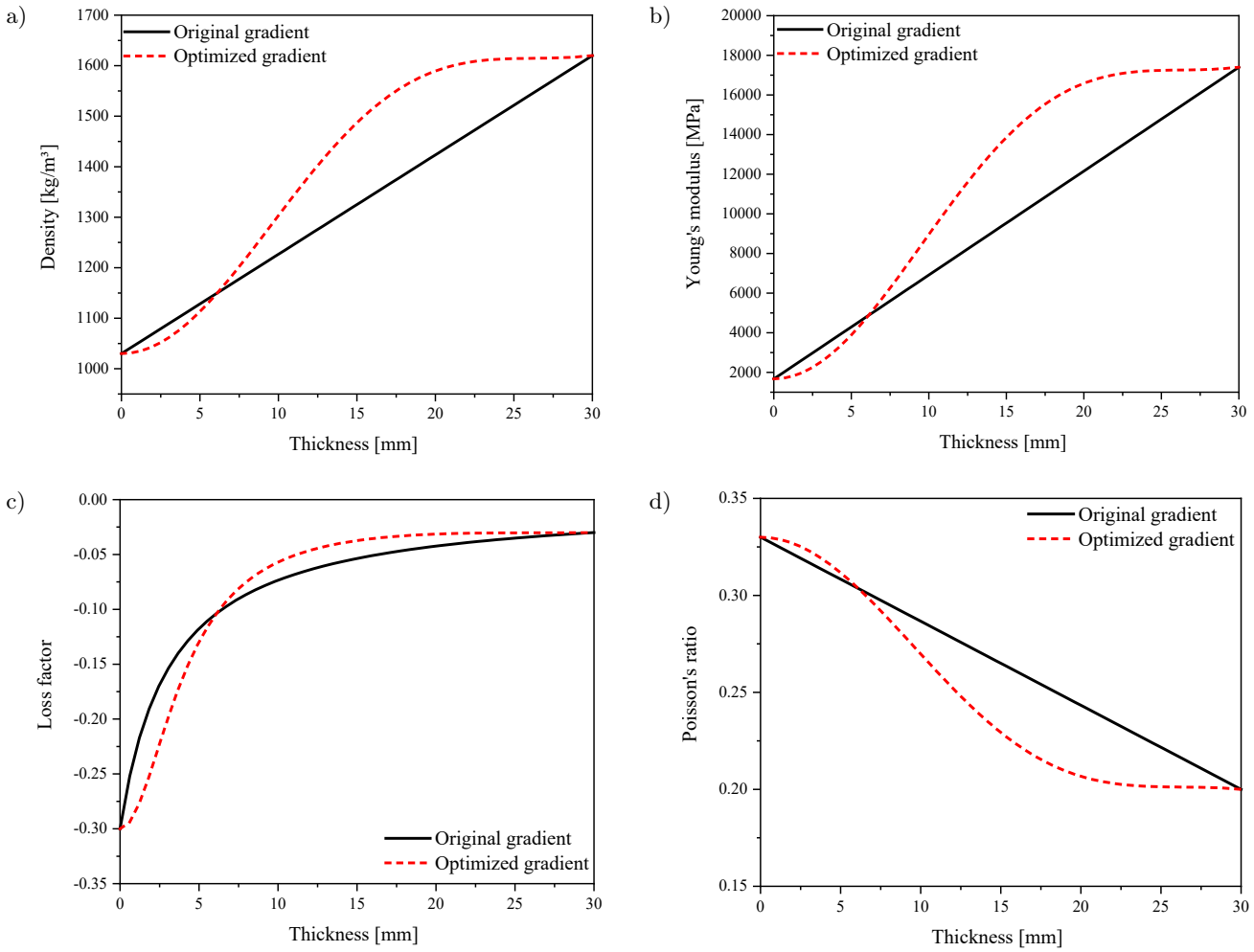

Fig. 13. Comparison results of the FRP-rubber FGM acoustic window before and after the turbulent self-noise suppression and sound transmission performance optimization: a) density; b) Young's modulus; c) loss factor; d) Poisson's ratio.

The comparison results of the self-noise suppression and sound transmission performance of the FRP-rubber FGM acoustic window before and after optimization are shown in Fig. 14.

Figure 14 shows that the optimized FGM acoustic window is superior to the initial linear FGM acoustic window in both turbulent self-noise suppression and sound transmission performance. From Fig. 14b, the peak value of the STL of the optimized FGM acoustic window compared to that of the initial linear FGM acoustic window decreases by approximately 0.6 dB at f = 10 kHz, which corresponds to a 12% increase in the sound transmission performance. Figure 14c shows that the turbulent self-noise reduction of the optimized FGM acoustic window is significantly higher than that of the initial FGM acoustic window. Moreover, the self-noise reduction gradually increases with increasing frequency, and the highest self-noise reduction is approximately 0.2 dB at f = 10 kHz, which corresponds to a 13% improvement in the turbulent self-noise suppression performance.

5. Analysis of the sound transmission and turbulent self-noise suppression characteristics of FGM acoustic windows before and after optimization

Section 4 indicates that the sound transmission and self-noise suppression performances of the optimized FGM acoustic window is improved. To analyze the reasons, mechanism studies of the sound transmission and turbulent self-noise suppression characteristics of the FRP-rubber FGM acoustic window are carried out.

5.1. Sound transmission analysis of FGM acoustic windows before and after optimization

To analyze the sound transmission mechanism of FGM acoustic windows, the dispersion curve of FRP is calculated based on the spectral method (Karpfinger *et al.*, 2008; 2010). The critical angles of various elastic waves under Snell's law are calculated based on

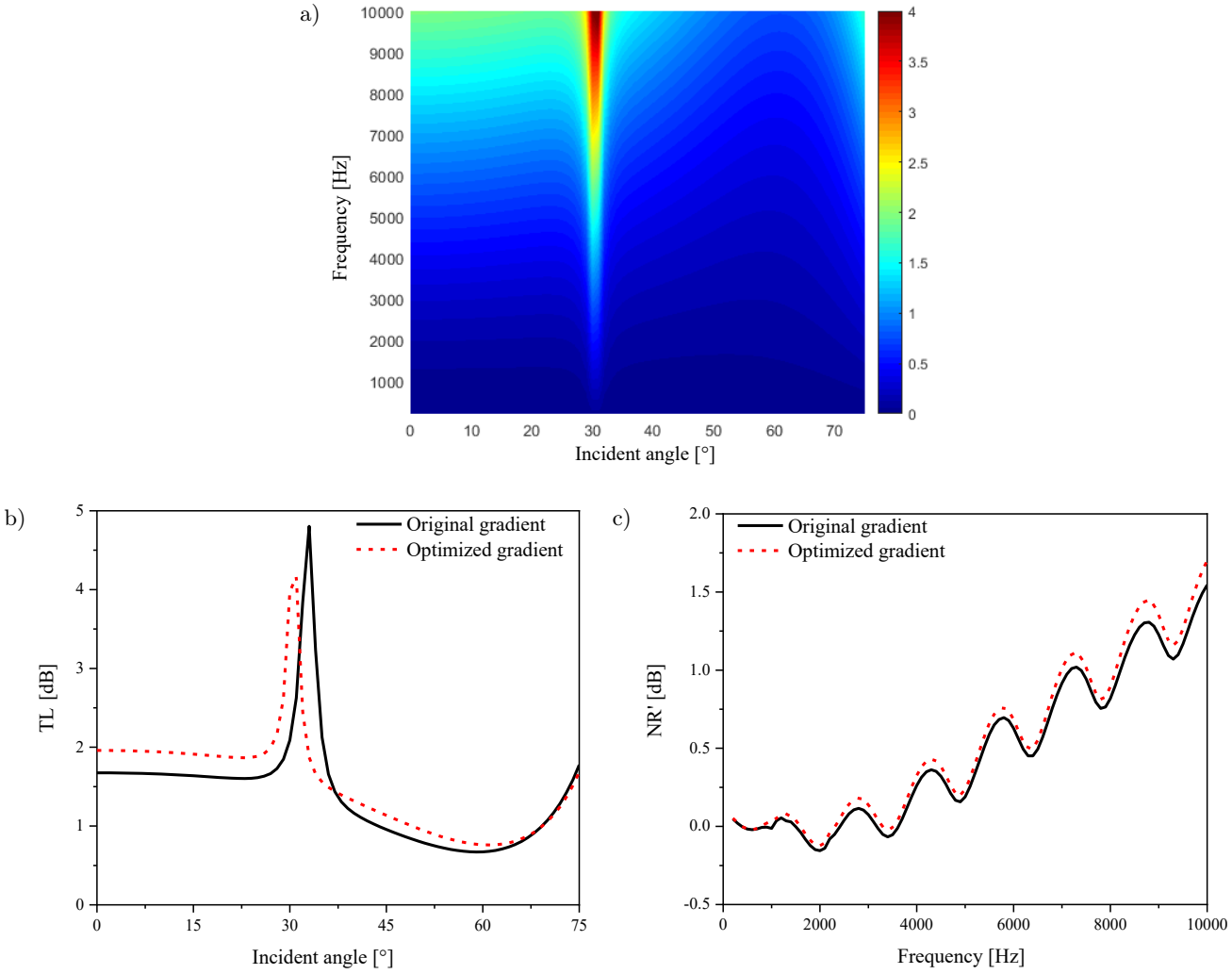

Fig. 14. Comparison results of the turbulent self-noise reduction and STL of the FRP-rubber FGM acoustic window before and after the turbulent self-noise suppression and sound transmission performance optimization: a) STL of the optimized FGM; b) STL at f = 10 kHz; c) comparison of the turbulent self-noise reduction.

the obtained phase velocity dispersion curve, as shown in Fig. 15.

The vertical narrow fringe with a strong STL appears near the critical angle (28°) of the total internal reflection of the longitudinal wave in the FRP. The longitudinal wave formed by the refraction of the incident wave propagates along the surface of the plate, and the critical angle corresponds to the velocity of the longitudinal wave. The curved fringe on the left of the critical angle is caused by the high-order Lamb surface wave in the elastic plate, of which the trajectory can be predicted according to the phase velocity of the high-order elastic wave. The internal material properties of the functional gradient materials gradually change along the plate thickness. The internal material properties of the functional gradient materials can be approximated as a single material by gradual changes along the plate thickness direction (Brekhovskikh, 2012). The equivalent Young's modulus E_e is:

$$E_e = \sum_{i=1}^{N} E_i h / H. \tag{31}$$

The other equivalent acoustic parameters are also calculated based on Eq. (31). Then, according to Eq. (31) and Snell's law, the equivalent longitudinal wave velocity $c_{Le}^2 = \frac{E_e}{(1-\sigma_e^2)\rho_e}$ and the estimated critical angle $\theta = \arcsin\left(\frac{c}{c_{Le}}\right)$ of the FGM acoustic windows before and after the optimization are shown in Table 6.

As shown in Table 6, the critical angle predicted by the equivalent longitudinal wave velocity is basically consistent with the actual critical angle, indicating that the peak value position of STL is derived from the critical angle of the equivalent longitudinal wave, which can be predicted precisely. To analyze the peak values of the STL of the FGM acoustic windows before and after optimization, thin-plate theory ignoring secondary factors is selected for analysis (Brekhovskikh, 2012). When the acoustic wave is

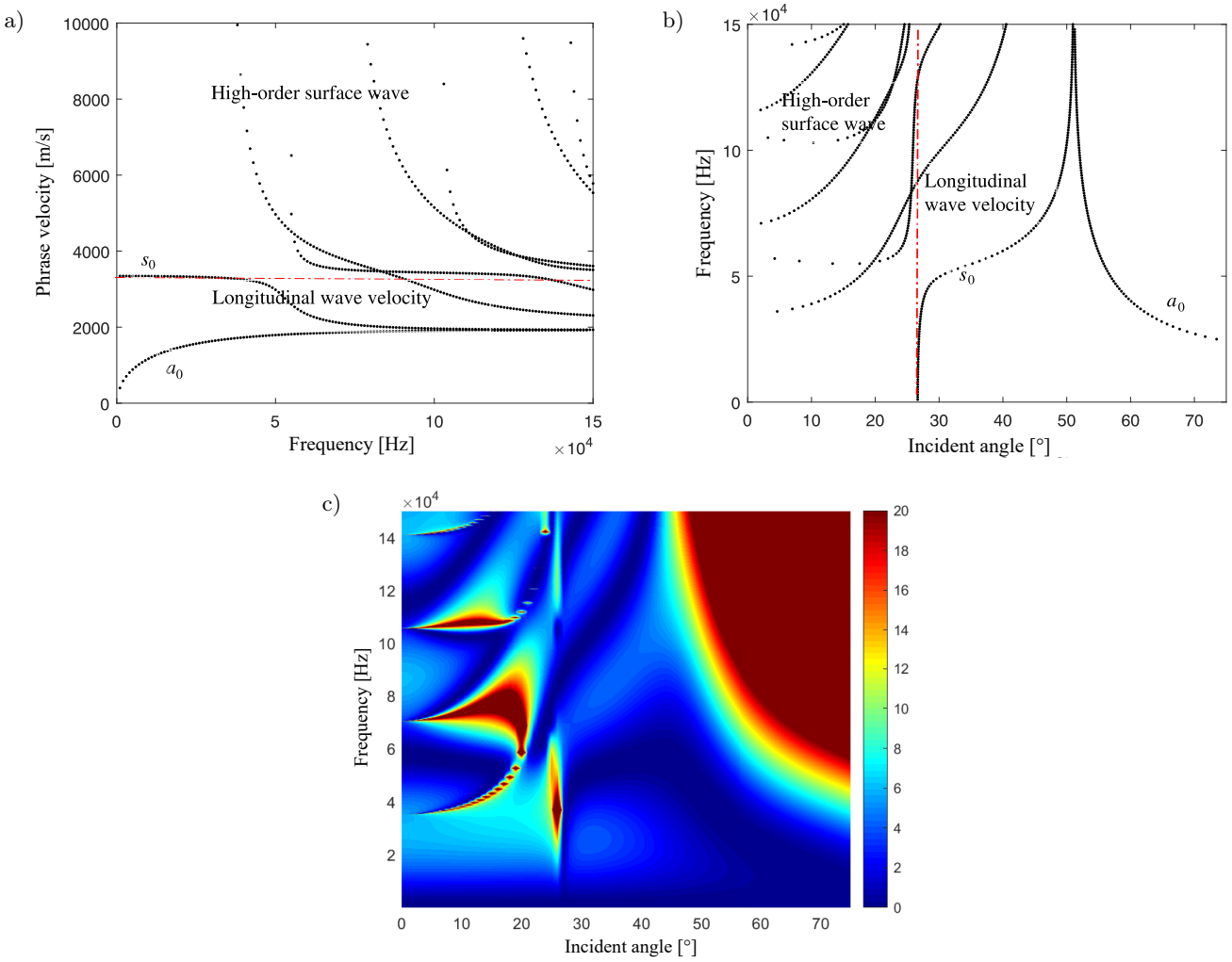

Fig. 15. Dispersion characteristics and STL results of the FRP: a) dispersion curve; b) critical angle of elastic waves; c) angle-frequency spectrum of STL.

Table 6. Equivalent longitudinal wave velocity and the estimated critical angle of the FGM acoustic windows before and after optimization.

	Equivalent longitudinal wave velocity c_{Le} [m/s]	Estimated critical angle θ [°]	Actual critical angle [°]
Origin	2782	32.6	32.7
Sound transmission performance optimization	2969	30.3	30.2
Self-noise reduction performance optimization	2781	32.6	32.9
Sound transmission and self-noise suppression	2971	30.2	30.7

incident at the critical angle of the longitudinal wave, the mechanical impedance of the longitudinal wave is $Z_s = 0$, and the transmission coefficient is:

$$\frac{1}{|W|^2} = \left|\frac{Z}{Z_a} + 1\right|^2, \tag{32}$$

where Z_a is the mechanical impedance of the shear wave, which is approximately $-i\omega m/2$ at the critical angle of the longitudinal wave; $Z = \rho c/\cos\theta$, where ρ and c are the density and acoustic velocity, respectively, and θ is the critical incident angle. Then, the STL is satisfied as:

$$\mathrm{STL} \propto 1 + \left(\frac{2\rho c}{\omega m \cos\theta}\right)^2. \tag{33}$$

Combined with the results in Figs. 9 and 13, the optimized FGMs have a larger equivalent mass m and a lower equivalent Poisson's ratio compared with the initial FGMs but also have a higher equivalent Young's

modulus. Compared with the magnitude difference of the equivalent Young's modulus, the density and Poisson's ratio changes are both minuscule. As a result, the equivalent longitudinal wave velocity increases, while the critical angle θ of the longitudinal wave decreases. Combined with Eq. (32), the peak value of the STL under the longitudinal wave critical angle will decrease.

The change in the STL before and after optimization at lower incident angles can be explained using the thin-plate theory (Morse, Ingard, 1986), as shown in Eq. (34):

$$\mathrm{TL} = 20\log\left|\frac{i\gamma}{\rho_{N+1}}\left(D\frac{k^4}{\omega^2} - m\right) + 2\right|, \tag{34}$$

where

$$\gamma = \sqrt{k_{N+1}^2 - k^2},$$

the bending stiffness is

$$D = \frac{E_e h^3}{12\left(1-\sigma_e^2\right)},$$

and m is the mass per unit length. By combining Eqs. (32) and (34), although the equivalent mass m is improved after optimization, the bending stiffness D is proportional to the equivalent Young's modulus and has the order of the fourth power of the wavenumber k. Therefore, the higher equivalent Young's modulus of the optimized FGM acoustic windows leads to an increase of the STL at lower incident angles. So, when the composition of the FRP in the FRP-rubber FGM acoustic window is increased, the corresponding equivalent Young's modulus is higher, which induces a decrease in the peak value of STL because Young's modulus of rubber is smaller than that of the FRP. A higher equivalent Young's modulus induces an STL decrease at the critical angle, a shift of the critical angle towards lower incident angles, and an increase in the STL at lower incident angles, but the total STL decreases, corresponding to better sound transmission performance.

5.2. Turbulent self-noise suppression characteristics of FGM acoustic windows before and after optimization

To analyze the reasons for the increase in the turbulent self-noise reduction of FGMs before and after optimization, the wavenumber-frequency spectrum results of the spatial filtering function are calculated at $R = 0.3$ and $L = 0.5$ m. Figure 16 shows the calculation results of FRP with $H = 3$ cm.

Three characteristic identification lines are clearly seen in Fig. 16. A relatively clear dividing line is formed between the lower left corner and the upper right corner of the figure, which corresponds to the acoustic wavenumber k_0 in water at each frequency. This is called the dividing line of the acoustic wavenumber,

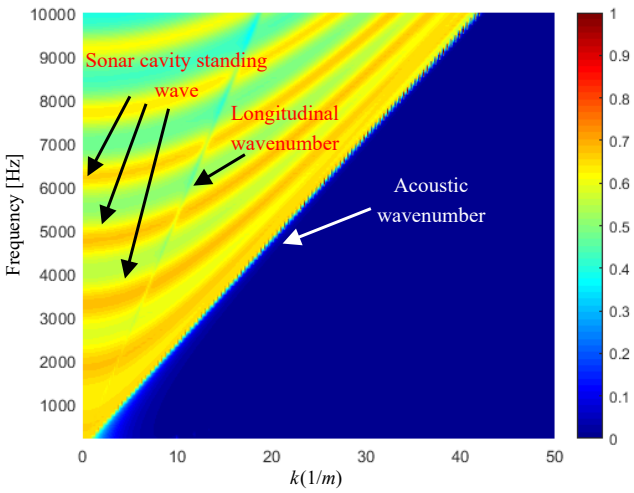

Fig. 16. Wavenumber-frequency spectrum results of the spatial filter function of FRP.

indicating that the spatial filter composed of the acoustic window and sonar cavity has the characteristics of a low-wavenumber passband and a high-wavenumber stopband. There is a lighter stripe from the lower left corner to the upper right corner, which corresponds to the longitudinal wavenumber of FRP. In addition, there are prominent periodic ripple lines in the figure, which are derived from the standing wave field formed in the sonar cavity by self-noise, and this feature is also the reason for the periodic fluctuation in the turbulent self-noise reduction. Figure 17 shows the wavenumber-frequency spectrum results of the spatial filtering function of the FGMs acoustic window before and after turbulent self-noise suppression and sound transmission performance optimization (STL and NR optimization).

As shown in Fig. 17, the corresponding equivalent longitudinal wave velocities of the FRP-rubber FGM acoustic windows before and after optimization are different according to Eq. (30), which results in different slopes of the characteristic lines of the longitudinal wavenumber. For the original FRP-rubber FGM, the reason for the small slope is that a small longitudinal wave velocity corresponds to a large wavenumber. Before and after optimization, the periodic fringe remains consistent because the acoustic medium and the height inside the sonar cavity remain unchanged. The resonance period of the standing wave field formed inside the sonar cavity meets the following requirements:

$$f = \frac{nc_{N+1}}{2L}, \tag{35}$$

where n is the number of fringe periods. Figures 12d and 14d show that an increase in the turbulent self-noise reduction of the FRP-rubber FGM acoustic window before and after optimization is positively correlated with the frequency. To analyze the reason for the increase in self-noise reduction, Fig. 18 shows the spa-

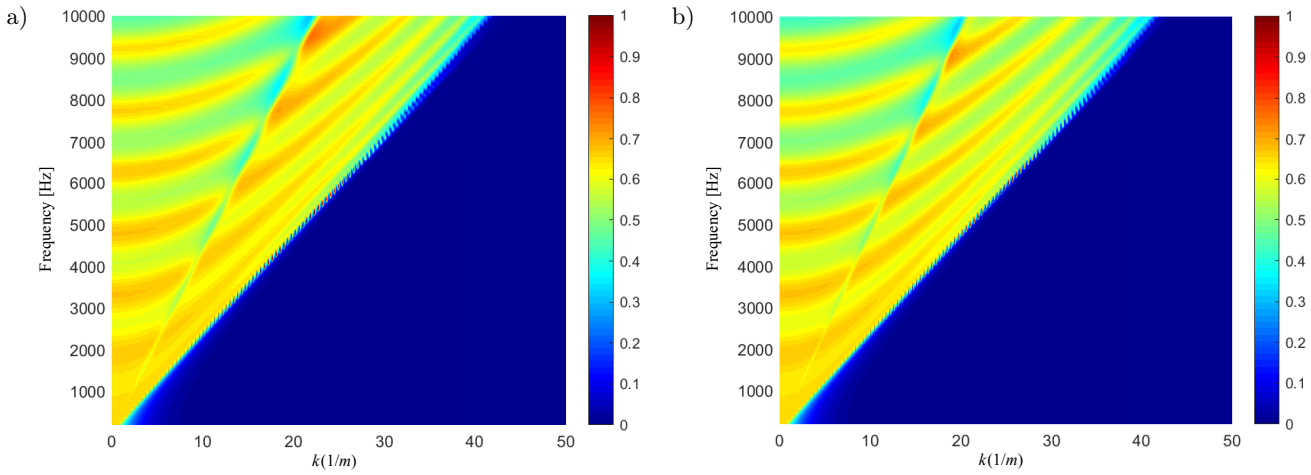

Fig. 17. Wavenumber-frequency spectrum of the spatial filtering function of the FRP-rubber FGM acoustic windows before and after optimization: a) original FGM; b) optimized FGM for STL and NR' optimization.

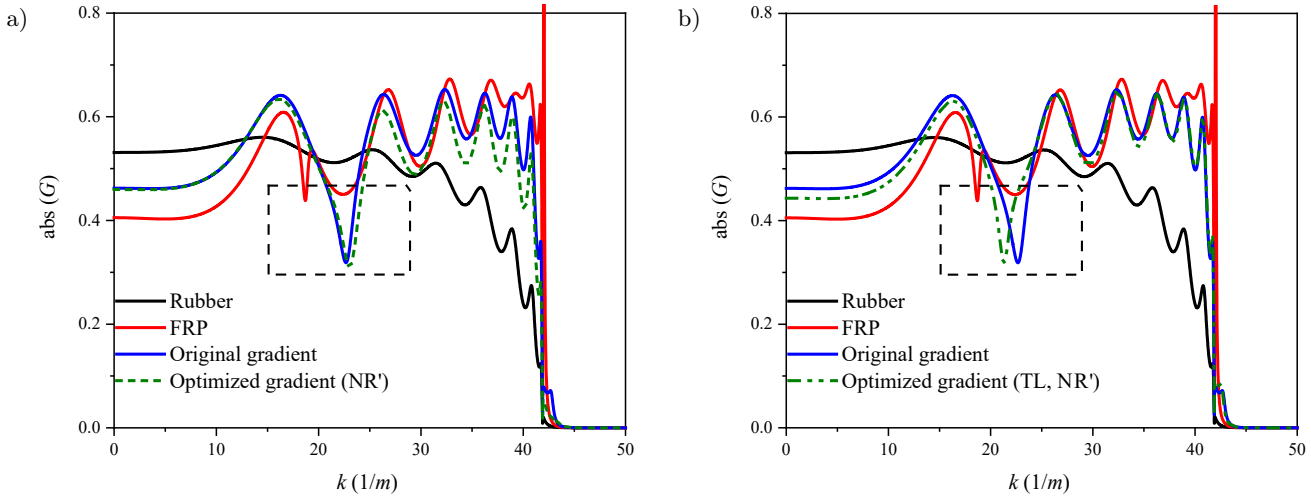

Fig. 18. Comparison of the spatial filtering functions of various acoustic windows at f = 10 kHz: a) FRP, rubber and FRP-rubber FGM acoustic window before and after the turbulent self-noise performance optimization (NR'); b) FRP, rubber and FRP-rubber FGM acoustic window before and after the turbulent self-noise and sound transmission performance optimization (TL, NR').

tial filtering function of the FRP-rubber FGM acoustic window before and after optimization at f = 10 kHz.

As shown in Fig. 18, the characteristic valley value is caused by the equivalent longitudinal wave of the various acoustic windows made from the FRP, rubber and FRP-rubber FGM before and after optimization. The original FRP-rubber FGM acoustic has a small equivalent longitudinal wave velocity corresponding to a large wavenumber of the characteristic value. For the optimized FRP-rubber FGM acoustic window, the equivalent longitudinal wave velocity is high, corresponding to a small wavenumber of the characteristic value. In addition, as shown in Figs. 18a and 18b, the rubber composition is beneficial for improving the filtering performance of higher wavenumbers, and the composition of FRP is beneficial for improving the filtering performance of lower wavenumbers in the region smaller than the acoustic wavenumber. The optimized specific ratio of rubber and FRP components brings about an FGM acoustic window with better filtering properties in the higher wavenumber region (Fig. 18b) and with better filtering properties in the lower wavenumber region (Fig. 18a), which can effectively suppress and shield the self-noise caused by the TBL pulsating pressure.

6. Conclusions

Considering the sonar self-noise suppression excited by the TBL pulsating pressure and sound transmission performance excited by the incident acoustic source for FGM acoustic windows, an internal gradient optimization method for FGMs is proposed in this paper, which can be used to design optimized FGM acoustic windows with better turbulent self-noise suppression abil-

ity and sound transmission performance. The theoretical modeling for FGM acoustic windows to evaluate the turbulent self-noise reduction and STL is completed in the proposed optimization method, in which the accuracy is verified by the finite element results of COMSOL Multiphysics. Using the optimization method proposed in this paper, the optimization calculations of the sound transmission performance, and the turbulent self-noise suppression performance, the sound transmission and turbulent self-noise suppression performance for the FRP-rubber FGM acoustic window are completed, and the results of the five optimization variables in the gradient function are separately obtained using the Bernstein polynomial as the deviation function. Finally, the mechanism of the sound transmission and turbulent self-noise suppression performance before and after optimization is explained based on the gradient material equivalent model and thin-plate model, respectively. The main conclusions are as follows.

The optimization results of the sound transmission performance, the self-noise suppression performance, and the sound transmission and self-noise suppression performance for the FRP-rubber FGM acoustic window show that the sound transmission or self-noise suppression performance of the optimized FGM acoustic window is effectively improved, indicating the effectiveness of the optimization method.

The peak position of the STL originates from the S_0 wave, which corresponds to the longitudinal wave velocity at the low frequency. The peak STL value and position and the STL at lower incident angles are mainly determined by the equivalent Young's modulus. Appropriately increasing the composition of the FRP can improve the equivalent Young's modulus, which is beneficial to improve the sound transmission performance of the FRP-rubber FGM acoustic window.

The periodicity of the turbulent self-noise reduction with frequency arises from the standing wave resonance inside the sonar cavity; the slope identification feature of the spatial filter function arises from the equivalent longitudinal wavenumber and the acoustic wavenumber.

A spatial filter consisting of an acoustic window and sonar cavity has the characteristics of a low wavenumber passband and a high wavenumber stopband. The spatial filtering performance of the sonar cover can be improved by optimizing the internal gradient form. In the lower wavenumber passband (less than the acoustic wavenumber), rubber enhances higher wavenumber filtering, while FRP is good for lower wavenumber filtering. The optimization results show that reasonable adjustment of the ratio of FRP and rubber can improve not only the sound transmission performance, but also the overall filtering performance, corresponding to improving the turbulent self-noise suppression performance.

The research results of this paper provide a reference value for the future design of FGM acoustic windows for sonar hoods.

Appendix

The matrix $\mathbf{I}$ is:

$$\begin{bmatrix} I_{11} & I_{12} & I_{13} & I_{14} \\ I_{21} & I_{22} & I_{23} & I_{24} \\ I_{31} & I_{32} & I_{33} & I_{34} \\ I_{41} & I_{42} & I_{43} & I_{44} \end{bmatrix}.$$

The elements in the matrix $\mathbf{I}$ in the layer l are:

$$I_{11} = ik\cos\left(\sqrt{k_{Ll}^2 - k^2}z\right),$$

$$I_{12} = k\sin\left(\sqrt{k_{Ll}^2 - k^2}z\right),$$

$$I_{13} = i\sqrt{k_{Tl}^2 - k^2}\cos\left(\sqrt{k_{Tl}^2 - k^2}z\right),$$

$$I_{14} = \sqrt{k_{Tl}^2 - k^2}\sin\left(\sqrt{k_{Tl}^2 - k^2}z\right),$$

$$I_{21} = -\sqrt{k_{Ll}^2 - k^2}\sin\left(\sqrt{k_{Ll}^2 - k^2}z\right),$$

$$I_{22} = -i\sqrt{k_{Ll}^2 - k^2}\cos\left(\sqrt{k_{Ll}^2 - k^2}z\right),$$

$$I_{23} = k\sin\left(\sqrt{k_{Tl}^2 - k^2}z\right),$$

$$I_{24} = ik\cos\left(\sqrt{k_{Tl}^2 - k^2}z\right),$$

$$I_{31} = -\left(\lambda_l k_{Ll}^2 + 2\mu\left(k_{Ll}^2 - k^2\right)\right)\cos\left(\sqrt{k_{Ll}^2 - k^2}z\right)i/\omega,$$

$$I_{32} = i\left(\lambda_l k_{Ll}^2 + 2\mu_l\left(k_{Ll}^2 - k^2\right)\right)\sin\left(\sqrt{k_{Ll}^2 - k^2}z\right)i/\omega,$$

$$I_{33} = 2\mu_l k\sqrt{k_{Tl}^2 - k^2}\cos\left(\sqrt{k_{Tl}^2 - k^2}z\right)i/\omega,$$

$$I_{34} = -2i\mu_l k\sqrt{k_{Tl}^2 - k^2}\sin\left(\sqrt{k_{Tl}^2 - k^2}z\right)i/\omega,$$

$$I_{41} = -2i\mu_l k\sqrt{k_{Ll}^2 - k^2}\sin\left(\sqrt{k_{Ll}^2 - k^2}z\right)i/\omega,$$

$$I_{42} = 2\mu_l k\sqrt{k_{Ll}^2 - k^2}\cos\left(\sqrt{k_{Ll}^2 - k^2}z\right)i/\omega,$$

$$I_{43} = -i\mu_l\left(k_{Tl}^2 - 2k^2\right)\sin\left(\sqrt{k_{Tl}^2 - k^2}z\right)i/\omega,$$

$$I_{44} = \mu_l\left(k_{Tl}^2 - 2k^2\right)\cos\left(\sqrt{k_{Tl}^2 - k^2}z\right)i/\omega,$$

where λ_l and μ_l represent the lame constant in the layer l.

Acknowledgments

This work was supported by the National Natural Science Foundation of China (the grant no. 11774229).

References

1. Brekhovskikh L. (2012), *Waves in Layered Media*, Elsevier.
2. Burton S.A. (1998), A cost effective solution for noise free GRP sonar domes in dynamic conditions, [in:] *UDT 1998 Conference Proceedings*, pp. 277–281.
3. Caiazzo A, Desmet W.A. (2016), A generalized Corcos model for modelling turbulent boundary layer wall pressure fluctuations, *Journal of Sound and Vibration*, **372**: 192–210, doi: 10.1016/j.jsv.2016.02.036.
4. Chandra N., Raja S., Gopal K.V.N. (2014), Vibro-acoustic response and sound transmission loss analysis of functionally graded plates, *Journal of Sound & Vibration*, **333**(22): 5786–5802, doi: 10.1016/j.jsv.2014.06.031.
5. Chandra N., Raja S., Gopal K.V.N. (2015), A comprehensive analysis on the structural–acoustic aspects of various functionally graded plates, *International Journal of Applied Mechanics*, **7**(5): 1550072, doi: 10.1142/S1758825115500726.
6. Cremer L., Heckl M., Petersson B. (2005), *Structure-borne Sound: Structural Vibration Sand Sound Radiation at Audio Frequencies*, Springer-Verlag.
7. Crighton D.G., Dowling A.P., Williams J.E., Heckl M., Leppington F.G. (1992), *Modern Methods in Analytical Acoustics*, Springer-Verlag, pp. 452–509.
8. George N., Pitchaimani J., Murigendrappa S., Lenin Babu MC. (2016), Vibro-acoustic behavior of functionally graded carbon nanotube reinforced polymer nanocomposite plates, [in:] *Proceedings of the Institution of Mechanical Engineers, Part L: Journal of Materials: Design and Applications*, **232**(7): 566–581, doi: 10.1177/1464420716640301.
9. Ham Y., Kim J., Chang H. (2018), A study on the improvement of adhesive mixing ratio about acoustic window for enhancing sonar performance of submarine, *Journal of the Korea Institute of Military Science and Technology*, **21**(4): 481–488, doi: 10.9766/KIMST.2018.21.4.481.
10. Hoffmann C. (1998), Integrated design approach for sonar domes, [in:] *UDT 1998 Conference Proceedings*, pp. 83–86.
11. Hosseini-Hashemi S., Zare M., Fadaee S.R. (2010), A new exact analytical approach for free vibration of Reissner–Mindlin functionally graded rectangular plates, *International Journal of Mechanical Sciences*, **53**(1): 11–12, doi: 10.1016/j.ijmecsci.2010.10.002.
12. Iqbal Z., Naeem M.N., Sulta N. (2009), Vibration characteristics of FGM circular cylindrical shells using wave propagation approach, *Applied Mathematics and Mechanics*, **208**: 237–248, doi: 10.1007/s00707-009-0141-z.
13. Karpfinger F., Gurevich B., Bakulin A. (2008), Modeling of wave dispersion along cylindrical structures using the spectral method, *The Journal of the Acoustical Society of America*, **124**(2): 859–865, doi: 10.1121/1.2940577.
14. Karpfinger F., Valero H.-P., Gurevich B., Bakulin A., Sinha B. (2010), Spectral-method algorithm for modeling dispersion of acoustic modes in elastic cylindrical structures, *Geophysics*, **75**(3): H19–H27, doi: 10.1190/1.3380590.
15. Kumar B.R., Ganesan N., Sethuraman R. (2009), Vibro-acoustic analysis of functionally graded elliptic disc under thermal environment, *Mechanics of Advanced Material & Structures*, **16**(2): 160–172, doi: 10.1080/15376490802625506.
16. Lane R. (1981), Absorption mechanisms for waterborne sound in Alberich Anechoic layers, *Ultrasonics*, **19**(1): 28–30, doi: 10.1016/0041-624X(81)90029-9.
17. Lavender M.A. (1994), The application of muti-layer modeling to dome design and hull treatments, [in:] *UDT 1994 Conference Proceedings*, pp. 296–299.
18. Lee J.-H., Kim B.-N., Shin K.-K., Yoon S.W. (2010), Insertion loss of sound waves through composite acoustic window materials, *Current Applied Physics*, **10**(1): 138–144, doi: 10.1016/j.cap.2009.05.017.
19. Liu Y., Compson C., Liu M. (2004), Nanostructured and functionally graded cathodes for intermediate temperature solid oxide fuel cells, *Journal of Power Sources*, **138**(1–2): 194–198, doi: 10.1016/j.jpowsour.2004.06.035.
20. Maidanik G. (1968), Domed sonar system, *The Journal of the Acoustical Society of America*, **44**(1): 113–124, doi: 10.1121/1.1911045.
21. Morse P.M., Ingard K.U. (1986), *Theoretical Acoustics*, Princeton University Press.
22. Mortensen A., Suresh S. (1995), Functionally graded metals and metal-ceramic composites: Part 1 processing, *International Materials Reviews*, **40**(6): 239–265, doi: 10.1179/imr.1995.40.6.239.
23. Pompe W. *et al.* (2003), Functionally graded materials for biomedical applications, *Materials Science and Engineering: A*, **362**(1–2): 40–60, doi: 10.1016/S0921-5093(03)00580-X.
24. Prakash T., Ganapath M. (2006), Asymmetric flexural vibration and thermoelastic stability of FGM circular plates using finite element method, *Composites Part B: Engineering*, **37**(7–8): 642–649, doi: 10.1016/j.compositesb.2006.03.005.

25. Rabbani V., Hodaei M., Dend X., Lu H., Hui D., Wu N. (2019), Sound transmission through a thick-walled FGM piezo-laminated cylindrical shell filled with and submerged in compressible fluids, *Engineering Structures*, **197**: 109323, doi: 10.1016/j.engstruct.2019.109323.

26. Shang E.C. (1965), An approximate formula for the wave reflection from gradual-transition absorbers [in Chinese], *ACTA Acustica*, pp. 192–197.

27. Skelton E.A., James J.H. (1997), *Theoretical Acoustics of Underwater Structures*, World Scientific.

28. Srivastava S.K. (1998), Ocean engineering aspects of submarine sonar dome, [in:] *UDT 1998 Conference Proceedings*, pp. 325–329.

29. Tang W.L., Yu M.S., Wang B. (2020), *Hydrodynamic Noise Theory* [in Chinese], Science Press.

30. Yu M.S., Li D.S., Gong L., Xu J. (2005), Design of sandwich acoustic window for sonar dome [in Chinese], *Chinese Journal of Acoustics*, **30**(5): 427–434, doi: 10.15949/j.cnki.0371-0025.2005.05.007.

31. Zhao X., Lee Y.Y., Liew K.M. (2009), Mechanical and thermal buckling analysis of functionally graded plates, *Composite Structures*, **90**(2): 161–171, doi: 10.1016/j.compstruct.2009.03.005.

32. Zhou L., Liu J.S., Hu H.H. (2020), Study on acoustic transmission performance of functionally gradient materials under turbulent excitation, [in:] *Noise and Vibration Control*, **40**(5): 71–75+88.